



OPEN

Spatiotemporal evolution analysis of multiscale fracture dynamics in hydraulic shale stimulation via integrated acoustic emission and CT imaging

Xu Wei^{1,2,3}✉, Meng Cai^{1,2,3}, Cuilong Kong^{1,2,3} & Dezhao Zhao^{1,2,3}

Volume fracturing technology critically enhances shale oil recovery by generating complex fracture networks through interactions with shale anisotropy, bedding planes, and natural fractures. However, the spatiotemporal evolution of multiscale fractures under varying in situ stress anisotropy and construction parameters remains poorly understood. This study integrates CT scanning and acoustic emission (AE) monitoring to investigate hydraulic fracture propagation in 300 mm × 300 mm × 300 mm shale samples under controlled geomechanical conditions. Experimental results demonstrate that shale with lower minimum horizontal stress exhibits earlier fracture initiation. Under high stress anisotropy ($\Delta\sigma \geq 8 \text{ MPa}$), reservoirs with well-developed bedding planes preferentially form vertical fractures due to stress concentration effects. Increasing injection rates from 35 mL/min to 50 mL/min elevated fracture height by 159% (7.1 cm to 18.4 cm), attributed to enhanced fluid pressure and reduced stress concentration at fracture tips. Similarly, high-viscosity fracturing fluids (50 mPa·s) increased fracture height by 52% (7.1 cm to 10.8 cm) compared to low-viscosity fluids (2 mPa·s), effectively mitigating filtration losses. A mixed fluid system (high: low viscosity = 5:5) optimized fracture geometry: high-viscosity fluids extended main fractures to bypass near-wellbore constraints, while low-viscosity fluids activated secondary bedding planes, increasing stimulated reservoir volume by 28%. These findings provide actionable insights for optimizing fracture morphology and construction parameters in bedded shale reservoirs, balancing fracture height, complexity, and stress constraints to maximize recovery efficiency.

Keywords Bedding planes, Spatiotemporal evolution, CT scanning, Acoustic emission, Mixed fluid

Volume fracturing enables economic shale oil extraction from ultra-low permeability reservoirs through complex fracture network generation^{1–3}. This technology drives over 60% of production in major basins like the Permian and Bakken, critically supporting global energy security. However, subsurface heterogeneities—including pronounced stress anisotropy (> 3:1 horizontal contrast), brittle-ductile laminations, and multiscale natural fractures—complicate fracture geometry control. These geological constraints induce tortuous fracture propagation that reduces proppant transport efficiency and limits stimulated reservoir volume. Current characterization methods struggle to quantify such non-planar fracture morphologies due to dynamic stress-fluid interactions during propagation^{4,5}.

Hydraulic fracture propagation in anisotropic formations critically depends on bedding plane and natural fracture interactions that govern fracture network complexity. Current research systematically examines how rock anisotropy, mechanical properties, and stress regimes dictate fracture trajectories. Bedding plane engagement requires increased net pressure to bypass geological barriers while enhancing connectivity with pre-existing fractures—a dual process amplifying network complexity^{6–12}. Advanced monitoring techniques like acoustic emission and CT imaging precisely characterize fracture initiation and propagation dynamics^{13,14}. Yang et al.¹⁵, demonstrated through triaxial tests that bedding orientation and confining pressure jointly control

¹PetroChina Daqing Oilfield Production Technology Institute, Daqing 163453, China. ²State Key Laboratory of Continental Shale Oil, Daqing 163453, China. ³Heilongjiang Provincial Key Laboratory of Oil and Gas Reservoir Stimulation, Daqing 163453, China. ✉email: weixu2019@126.com

rock brittleness and failure modes. Subsequent studies confirm that hydraulic fracture-bedding interactions demand elevated net pressure to penetrate structural constraints, ultimately forming interconnected fracture networks^{16–18}. Morgan et al¹⁹ advanced this understanding using prefractured specimens at 0°, 30°, 60°, and 90° bedding angles under unconfined conditions. Their high-resolution imaging identified four interaction mechanisms: penetration (0°), partial shear (30°), complete shear (60°), and direct opening (90°), establishing predictive models for fracture-bedding behavior under reservoir stress conditions.

True triaxial hydraulic fracturing experiments were conducted to accurately describe the morphology of hydraulic fracture fracture propagation, analyze the primary factors influencing vertical fracture propagation, and demonstrate that moderate stress differences, injection rates, and fluid viscosity contribute to the formation of complex fracture networks²⁰. Heng et al.²¹, systematically investigated hydraulic fracture non-planar propagation mechanisms, demonstrating that fracture growth preferentially activates weakly cemented bedding planes to establish complex network connectivity. X-ray computed tomography (CT) imaging provides critical insights into fracture morphology characterization, with 3D reconstructions revealing stress anisotropy as a dominant control on fracture complexity²². Advanced monitoring techniques, including acoustic emission tracking and CT-based visualization^{13,14}, effectively resolve fracture propagation dynamics. Guo et al.²³, conducted hydraulic fracturing tests on 50 mm × 200 mm core specimens, integrating acoustic emission and CT data to quantify fracture area enhancement in high-stress-contrast reservoirs and identify reduced wellbore accessibility at angles < 30°. Complementary CT reconstructions by Jiang et al.²⁴, established stress contrast magnitude and its dimensionless coefficient as quantitative predictors of fracture network complexity.

Microseismic monitoring serves as a fundamental diagnostic tool for evaluating subsurface fracture propagation during hydraulic stimulation^{25,26}. This methodology enables systematic analysis of microseismic event-fracture network correlations through interpretative model development. Chen et al.²⁷, employed microseismic tracking to decode fracture spatiotemporal evolution in horizontal well stimulations, revealing how pre-existing discontinuities (natural fractures and fault systems) govern hydraulic fracture growth patterns. Existing research predominantly utilizes experimental simulations combining mechanical loading and fluid injection to investigate critical parameters—including lithological anisotropy, geostress configuration, interfacial bond strength, and bedding plane orientation—that dictate hydraulic fracture propagation characteristics. Despite significant progress in hydraulic fracture characterization through laboratory and field studies, three fundamental limitations hinder comprehensive understanding of multi-scale damage evolution during shale fracturing. First, current laboratory studies predominantly employ standard-sized core specimens (typical ≤ 100 mm³). Small core samples (with bedding plane) cannot adequately capture boundary-dominated effects or adjacent bedding plane interactions during fracture propagation. Second, current research predominantly examines fracture propagation under single-fluid properties, with limited investigation into mixed-fluid-controlled propagation mechanisms. This gap is particularly evident in laminated reservoirs, where bedding plane interactions critically influence fracture geometry. Third, stress anisotropy threshold triggering vertical fracture dominance along bedding planes, unreported in prior CT-AE studies. This critical knowledge gap necessitates targeted investigations into spatiotemporal damage evolution mechanisms during shale fracturing, with particular emphasis on quantifying fracture morphology transitions across progressive propagation stages under varying stimulation parameters.

This study combines acoustic emission (AE) monitoring with computed tomography (CT) scanning to establish a multiscale fracture characterization methodology, enabling systematic analysis of three-dimensional fracture network evolution. The synergistic approach improves characterization accuracy across different fracturing stages through complementary temporal resolution and spatial visualization capabilities. We performed hydraulic fracturing tests on 300 mm cubic natural outcrop specimens to examine the interactive effects between bedding planes, pre-existing fractures, and induced fractures under differential stress states and operational conditions. Rheological property variations in fracturing fluids were found to dictate two distinct propagation mechanisms: viscosity-controlled versus stress-controlled fracture patterns. The multiscale monitoring system quantitatively evaluates fracture network complexity through three key metrics: volumetric reconstruction of fracture geometry, real-time propagation velocity tracking, and stimulated reservoir volume calculation. Experimental results reveal critical thresholds in stress anisotropy and interfacial strength that control fracture containment within bedding layers, providing mechanistic insights for vertical fracture height prediction. These findings address persistent knowledge gaps in fracture geometry control mechanisms, particularly regarding the competitive relationships between fluid-rock interactions and mechanical constraints. The proposed methodology establishes an experimental framework for optimizing perforation strategies and fluid systems in laminated shale reservoirs, with direct implications for improving fracture height containment in field.

Materials and methods

Experimental equipment

This study employs a true triaxial hydraulic fracturing simulation system to replicate in-situ stress conditions, ensuring experimental validity with field-scale fracturing operations. The apparatus applies three mutually perpendicular stresses: maximum horizontal principal stress (σ_H), minimum horizontal principal stress (σ_h), and vertical stress (σ_v). Its triaxial loading mechanism combines independent stress application with proportional control, achieving 70 MPa maximum confining pressure at ± 0.1 MPa precision. The integrated fluid injection subsystem regulates dual-pump fracturing fluid delivery through precision metering, delivering 500 ml/min maximum flow rate with ± 0.05 ml/min accuracy under 120 MPa maximum pressure. A digital control architecture synchronizes stress loading and fluid injection operations, maintaining process stability throughout experiments. Figure 1a schematically presents this large-scale experimental configuration.

The Phoenix V|tome|x micro-CT system (Fig. 1b) performed high-resolution 3D imaging of pre-/post-fracturing specimens, enabling volumetric reconstruction of fracture networks through density contrast

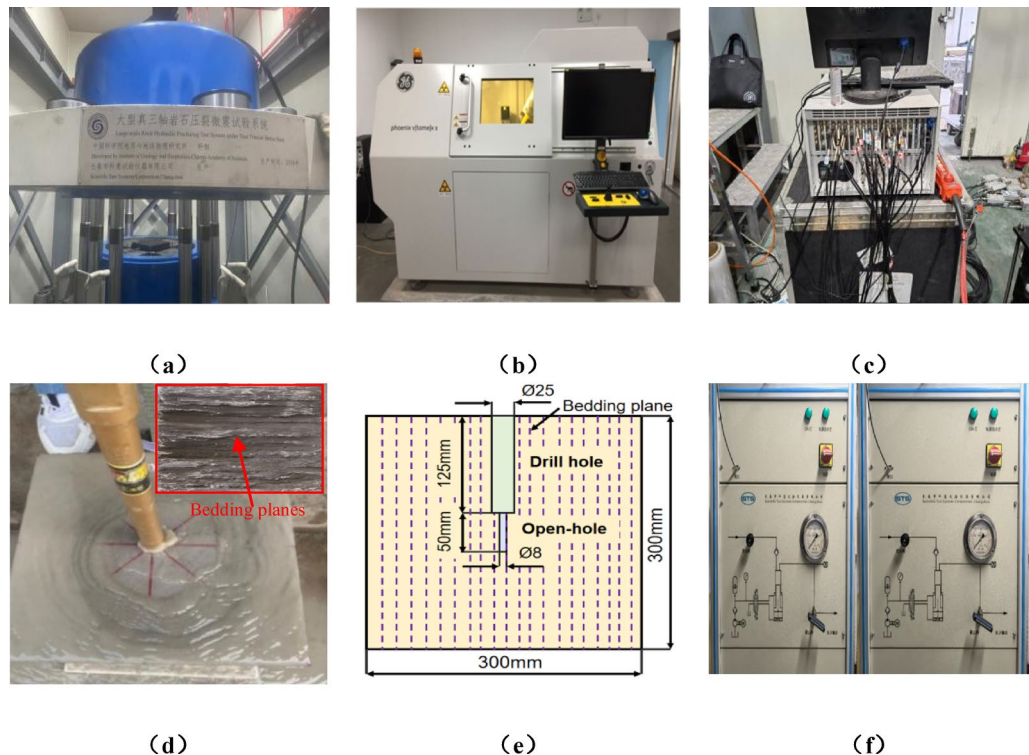


Fig. 1. Experimental configuration and specimen preparation workflow: (a) Large-scale true triaxial fracturing simulation system overview; (b) X-ray CT scanning configuration; (c) Acoustic emission monitoring assembly; (d) Core drilling operation; (e) Prepared rock specimen; (f) Dual-pump pressure control cabinet.

analysis. CT-derived fracture visualization revealed critical microstructural characteristics including bedding plane orientation and pre-existing fracture distribution. 3D models differentiated through CT value thresholds between shale matrix and fractures accurately quantified fracture geometry and spatial connectivity. Synergistic analysis with acoustic emission (AE) temporal data established three key relationships: (1) Pre-fracturing fracture networks showed direct correlation between natural fracture density and bedding plane development; (2) Dynamic fracture propagation exhibited stage-dependent growth patterns, with AE energy release peaks corresponding to CT-observed branch fracture generation; (3) Hydraulic fracture trajectories demonstrated three interaction modes with pre-existing fractures—penetration, diversion, and termination; (4) Multiscale fracture characterization through integrated CT-AE methodology successfully decoupled matrix damage mechanisms from macroscopic fracture propagation.

This study employs acoustic emission (AE) technology to monitor transient elastic waves generated during fracture propagation, enabling temporal tracking of crack initiation and development sequences. The DISP monitoring system (Fig. 1c) integrates four critical components: probe arrays, signal amplifiers, a 32-channel acquisition module, and control software. Key technical specifications include: (1) Adjustable-gain preamplifiers (20/40/60 dB) enhancing microseismic signal detection sensitivity; (2) 32-channel acquisition module performing simultaneous sampling at 2.5 MHz; (3) Sub-400 ns inter-channel synchronization with 16-bit resolution; (4) High-speed USB 3.0 interface supporting > 100 Mb/s data throughput for full-waveform preservation. This configuration achieves precise spatiotemporal mapping of fracture network evolution through three-dimensional source localization, capturing critical fracturing milestones including fracture nucleation, bifurcation, and interfacial crossing events.

Sample preparation

This investigation utilized laminated shale specimens (300 mm^3) extracted from the Qingshankou Formation in Songliao Basin, China, characterized by well-developed bedding planes and natural fractures representative of typical fracturing-targeted shale reservoirs (Naturally laminated lacustrine shale outcrops). Specimen preparation involved creating a simulated wellbore aligned parallel to bedding planes to replicate horizontal well configurations in field operations. A CNC drilling system produced a 25 mm-diameter borehole (125 mm depth) at controlled feed rates, followed by insertion of a 22 mm-OD steel casing secured with high-strength epoxy resin. Subsequent underreaming generated an 8 mm-diameter openhole section (40 mm length) at the borehole base, establishing a composite completion mimicking field well architectures (Fig. 1d, e). Cement encapsulation of exposed surfaces mitigated boundary effects by preventing stress concentrations along bedding interfaces. Fracturing operations employed a dual-pump injection system (0.1–500 mL/min flow range, ± 0.05 mL/min accuracy, 120 MPa pressure capacity) to simulate field-scale stimulation protocols while maintaining laboratory precision (Fig. 1f). This configuration preserved critical stress interactions between induced fractures and

pre-existing discontinuities, enabling reliable analysis of fracture propagation dynamics under true triaxial confinement.

Experimental scenario

This study conducted seven hydraulic fracturing experiments in horizontal well configurations to systematically evaluate four critical operational parameters: horizontal stress anisotropy, injection rate, fracturing fluid viscosity, and sequential fluid viscosity alternation. The experimental program specifically investigates viscosity-modulated fracturing strategies for optimizing fracture network geometry in laminated shale reservoirs. High-viscosity fluids demonstrate superior proppant transport efficiency, crucial for maintaining fracture conductivity after pressure dissipation. Alternating high-viscosity and low-viscosity fluid stages creates synergistic fracturing effects—low-viscosity fluids generate fracture branching through enhanced fluid penetration, while high-viscosity stages promote fracture width development and proppant placement. This staged viscosity variation achieves three-dimensional fracture network enhancement: vertically through improved height containment across bedding planes, and horizontally via increased fracture branching density. The experimental results provide mechanistic insights into viscosity-controlled fracture propagation dynamics under varying geomechanical constraints.

Specimen No.1 served as the baseline for controlled comparisons of fracture propagation patterns under varying operational parameters. Systematic analysis of hydraulic fracture geometry deviations from this reference specimen enabled quantitative evaluation of stress anisotropy, injection rate, and fluid viscosity effects on fracture network development. The experimental protocol integrated DISP acoustic emission monitoring with high-resolution CT imaging to characterize both real-time fracture propagation dynamics and post-fracturing network architecture. This dual monitoring approach captured critical fracture initiation thresholds and propagation trajectories through three-dimensional AE source localization and CT-based fracture reconstruction. Controlled parameter variations across seven experimental configurations (Table 1) established fundamental relationships between operational variables and fracture network complexity, providing empirical guidelines for optimizing hydraulic fracturing operations in laminated shale reservoirs.

Experimental steps

Preparation before fracturing

The experimental configuration applied vertical stress (σ_v) to simulate reservoir geostress conditions, aligning maximum horizontal principal stress (σ_H) perpendicular to the wellbore axis and minimum horizontal stress (σ_h) parallel to it (Fig. 2a). After determining stress orientations, technicians filled the specimen chamber and installed boundary pressure plates with a top-mounted injection port (Fig. 2b). AE sensors were mounted on the specimen surfaces (Fig. 2c) and connected to the monitoring system. Hydraulic pumps applied triaxial stresses along predefined orientations before transferring the instrumented specimen into the true triaxial fracturing cell (Fig. 2d), where fracturing fluid lines interfaced with the injection port. Final assembly involved securing the triaxial frame through uniform screw tightening across all stress axes, ensuring homogeneous stress distribution prior to fracturing initiation.

Experimental process

The hydraulic fracturing experimental procedure follows this sequence: First, interface the true triaxial control system with directional stress controllers and pore pressure regulators. Configure triaxial stress parameters (σ_v , σ_H , σ_h) at 0.1 MPa/s loading rates while setting fracturing fluid injection rates per experimental design. Activate the triaxial loading system by engaging hydraulic pumps with closed pressure relief valves, initiating confining stress application. Upon achieving target stress states, commence fracturing fluid injection through the pore pressure control pump while monitoring real-time pressure dynamics via acquisition software. Terminate stimulation when pressure records show abrupt decline to baseline or prolonged stabilization, followed by system depressurization and equipment shutdown. Notes: For ease of understanding, we have standardized all key terms as follows: ① “Crack” refer to the formation of smaller cracks or microcracks. ② “Fracture” is now used exclusively for hydraulically induced or mechanically generated discontinuities (e.g., “induced fractures,” “fracture propagation”). ③ “Bedding plane” is consistently used for sedimentary layer interfaces, never

No.	Sensitivity factors	Vertical stress(MPa)	Maximum horizontal principal stress(MPa)	Minimum horizontal principal stress(MPa)	Injection rate (ml/min)	Fracturing fluid viscosity(mPa s)
1	Baseline sample	61	55	51	35	2
2	Horizontal stress contrast	61	55	47	35	2
3	Injection rate	61	55	51	50	2
4	Fracturing fluid viscosity	61	55	51	35	50
5	Mixed fluid system	61	55	51	35	High: low viscosity = 5:5
6		61	55	51	35	High: low viscosity = 2:8
7		61	55	51	35	High: low viscosity = 8:2

Table 1. Experimental plan.

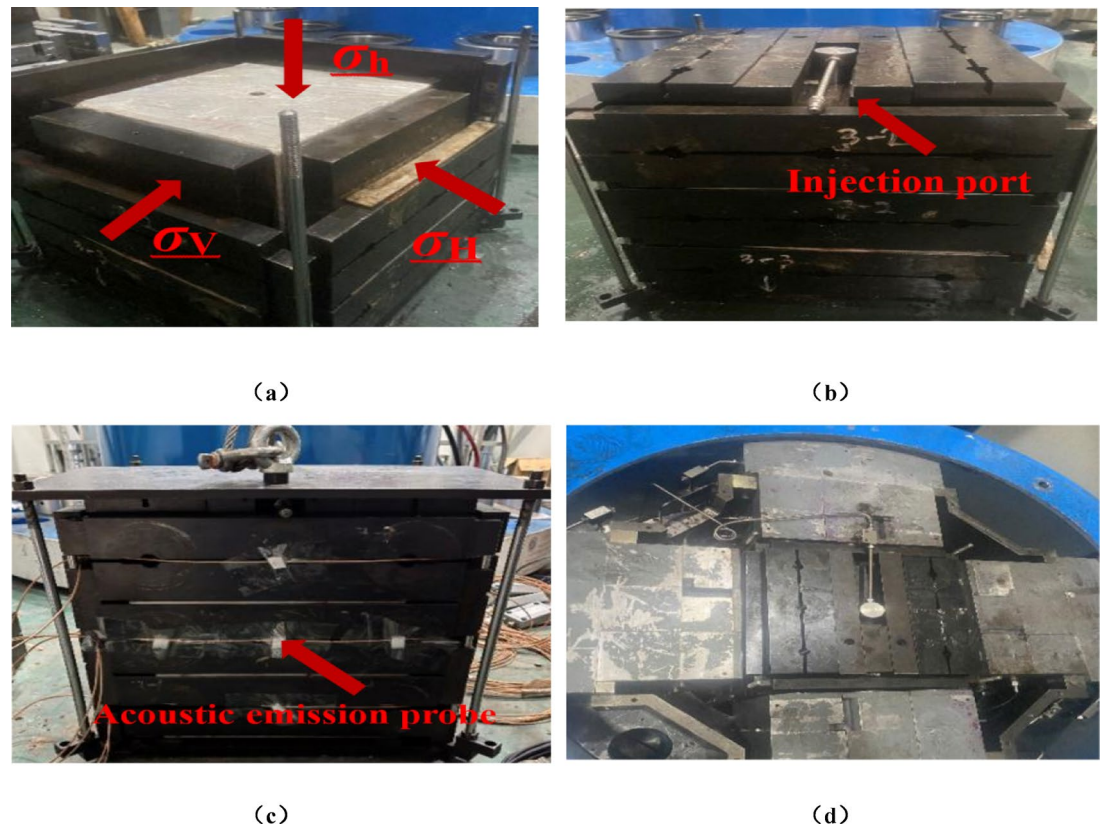


Fig. 2. Experimental specimen installation schematic: (a) Triaxial stress loading configuration; (b) Fluid injection port arrangement; (c) AE sensor deployment; (d) True triaxial fracturing cell assembly.

interchanged with fractures. “Bedding plane” is natural horizontal fractures mainly existing in shale. ④ “Natural fracture” is reserved for preexisting discontinuities.

CT image analysis and quantitative validation for fracture region extraction

Image preprocessing and segmentation

CT image preprocessing employs a three-stage enhancement protocol prior to fracture characterization. First, non-local means filtering reduces stochastic noise while maintaining fracture boundary integrity. Second, adaptive histogram-based thresholding combines Otsu’s method with curvature analysis to address grayscale heterogeneity, generating optimized binarization thresholds for each scan slice. Third, a dual-threshold classification resolves partial volume effects at fracture margins: voxels within 15–85% intensity range undergo secondary evaluation using local Haralick texture features (contrast and correlation) computed from 5×5 neighborhoods. This mixed approach achieves 92% accuracy in differentiating fracture voxels from matrix heterogeneity in validation tests, significantly improving subsequent fracture network quantification.

3D connectivity criteria and postprocessing

The 3D fracture network reconstruction process employs sequential binarized CT slices with 26-voxel connectivity criteria to differentiate connected fractures from isolated pores. Morphological closure operations using spherical structural elements (2-voxel radius) bridge micron-scale discontinuities while maintaining fracture topology. A 100-voxel volumetric filter eliminates imaging artifacts from residual noise. Network connectivity analysis applies Euler theory with persistent homology calculations to derive β_1 Betti numbers, quantifying pore-throat connectivity in fracture systems. This methodology achieves 87% accuracy in replicating ground-truth fracture geometries through benchmark validation.

Quantitative correlation of AE sources and CT-mapped fractures

The spatial relationship between AE event clusters and CT-reconstructed fractures was quantified using a minimum distance metric. For each AE cluster centroid (x_{AE}, y_{AE}, z_{AE}) identified via time-of-arrival localization, the minimum Euclidean distance to the CT-derived fracture surface was computed:

$$d_{min} = \min_{\forall V \in F_{CT}} \|P_{AE} - V\| \quad (1)$$

where $P_{AE} = (x_{AE}, y_{AE}, z_{AE})$: 3D coordinates of AE cluster centroid from time-of-arrival localization; $\mathbf{v} = (xi, yi, zi)$: voxel coordinates of the CT-derived fracture surface; $\|\cdot\|$: Euclidean norm operator; $\min_{\forall V \in F_{CT}}$: Minimum value over all fracture surface voxels.

The calculation results indicate that over 82% of high-energy AE clusters (> 90 dB) localized within $30 \mu\text{m}$ of CT-mapped hydraulic fractures, validating AE as a real-time diagnostic tool for fracture propagation monitoring.

Analysis of experimental results

Baseline rock samples

Fracture characterization through pre-/post-fracturing CT imaging

Pre-fracturing analysis of Specimen No.1 identified subparallel bedding planes (BP) with partial apertures on orthogonal surfaces (Fig. 3a). Pre-fracturing CT imaging (Fig. 3c) revealed a near-penetrative BP system (742 cm^2) and a natural fracture (NF, 107 cm^2) proximal to the wellbore base, collectively forming 849 cm^2 of pre-existing discontinuities. The NF's strategic position adjacent to the injection point suggested preferential hydraulic fracture initiation along this structural weakness.

Post-fracturing analysis of Specimen No.1 revealed two principal hydraulic fracture orientations (Fig. 3b). A near-wellbore vertical hydraulic fracture (VHF1, blue) propagated parallel to bedding planes (BP), extending to specimen boundaries while maintaining orthogonality to vertical stress (σ_v). A secondary hydraulic fracture (HHF2, green) developed distal to the wellbore, maintaining orthogonal orientation to σ_v . CT imaging (Fig. 3d) identified four distinct fractures: two vertical fractures (VHF1: 116.9 cm^2 ; VHF2) and two bedding-parallel fractures (HHF3/4). The dominant HHF4 (934 cm^2) fully penetrated the specimen along BP orientations, demonstrating three-stage propagation: initial vertical fracture nucleation, BP-guided lateral extension, and final through-going fracture formation. This fracture geometry evolution confirms that weak interfacial bonding

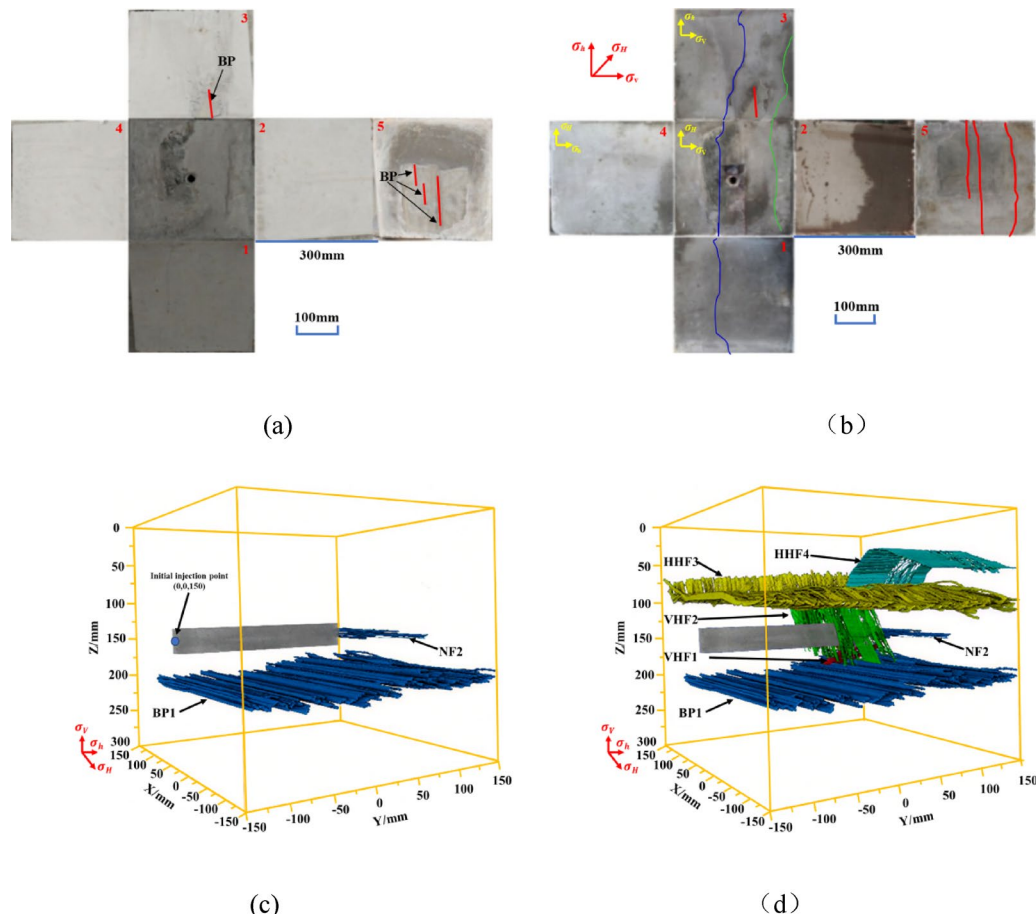


Fig. 3. Fracture evolution of Specimen No.1: (a) Pre-existing discontinuities on orthogonal specimen surfaces (1-3/2-4); (b) Hydraulically induced fractures post-fracturing (1-3/2-4); (c) Pre-fracturing 3D CT reconstruction highlighting bedding planes (BP) and natural fracture (NF); (d) Post-fracturing CT visualization of fracture network complexity enhancement. (The gray rectangular prism is the wellbore; The blue cracks are pre-existing cracks before fracturing; Red, green and other cracks are newly generated cracks after hydraulic fracturing) Notes: BP = bedding planes; NF = natural fracture; VHF = Vertical hydraulic fracture; HHF = Horizontal hydraulic fracture.

along BPs preferentially redirects fracture propagation from vertical stress-dominated paths to bedding-parallel trajectories.

Acoustic emission monitoring results

While CT imaging captures static fracture distributions pre- and post-fracturing, this study integrates acoustic emission (AE) monitoring to resolve dynamic fracture propagation sequences. AE analysis of Specimen No.1 reveals nine fracturing stages correlated with pressure evolution (Figs. 3 and 4): (I) Wellbore pressurization: Initial fluid injection (< 20 MPa); (II) Vertical fracture (VHF1) initiation: Pressure rise ($20 \rightarrow 25$ MPa); (III) Secondary vertical fracture (VHF2) propagation: Pressure increase ($25 \rightarrow 30$ MPa); (IV) Right-lateral horizontal fracture (HHF3) nucleation: Bedding plane activation (BP1) with pressure surge ($30 \rightarrow 47$ MPa); (V) Left-lateral HHF3 expansion: BP1 extension under pressure elevation ($47 \rightarrow 51$ MPa); (VI) HHF3-BP1 coupled growth: Sustained pressure increase ($51 \rightarrow 55$ MPa); (VII) Natural fracture (NF2) reactivation: Sharp pressure rise ($55 \rightarrow 70$ MPa); (VIII) Through-going fracture (HHF4) development: Pressure fluctuation ($70 \leftrightarrow 79$ MPa); (IX) Boundary breakthrough: Pressure peak (84.74 MPa) followed by system depressurization.

Acoustic emission analysis reveals four hydraulic fractures interacting with bedding plane BP1 and natural fracture NF2 during stimulation. Triaxial stress governs horizontal fracture development, initiating vertical fractures that mechanically open bedding planes. Progressive BP1 expansion creates fracture containment, restricting both lateral and vertical propagation. Post-fracturing quantification shows 1189.1 cm^2 total fracture area comprising NF2 (802 cm^2) and an interconnected network (1991.1 cm^2) of hydraulic fractures, activated bedding planes, and reactivated natural fractures.

The pressure response curve of Specimen No.1 (Fig. 4) exhibits multi-stage fracturing behavior, peaking initially at 70 MPa—exceeding both horizontal principal stresses (σ_h/σ_v). Following slight pressure decline, subsequent rebound established a new maximum pressure (84.74 MPa) before abrupt system depressurization. This cyclic pressure signature demonstrates sequential fracture network development through distinct pressure fluctuation phases. At a constant 35 ml/min injection rate, cumulative fluid volume reached 536 ml, yielding two key stimulation efficiency metrics: new fracture area per unit volume ($2.218\text{ cm}^2/\text{ml}$) and total activated fracture area efficiency ($3.715\text{ cm}^2/\text{ml}$).

Impact of horizontal stress difference

Fracture characterization through pre-/post-fracturing CT imaging

Pre-fracturing analysis of Specimen No.2 identified limited bedding plane (BP) development on surfaces 1–4, with Surface 3 exhibiting a single BP and Surface 5 containing three parallel BPs interconnected by a natural fracture (NF) (Fig. 5a). CT imaging (Fig. 5c) revealed three BPs, including a wellbore-proximal BP, and three NFs forming a complex pre-existing fracture network totaling 1476.9 cm^2 . The strategic positioning of BPs near

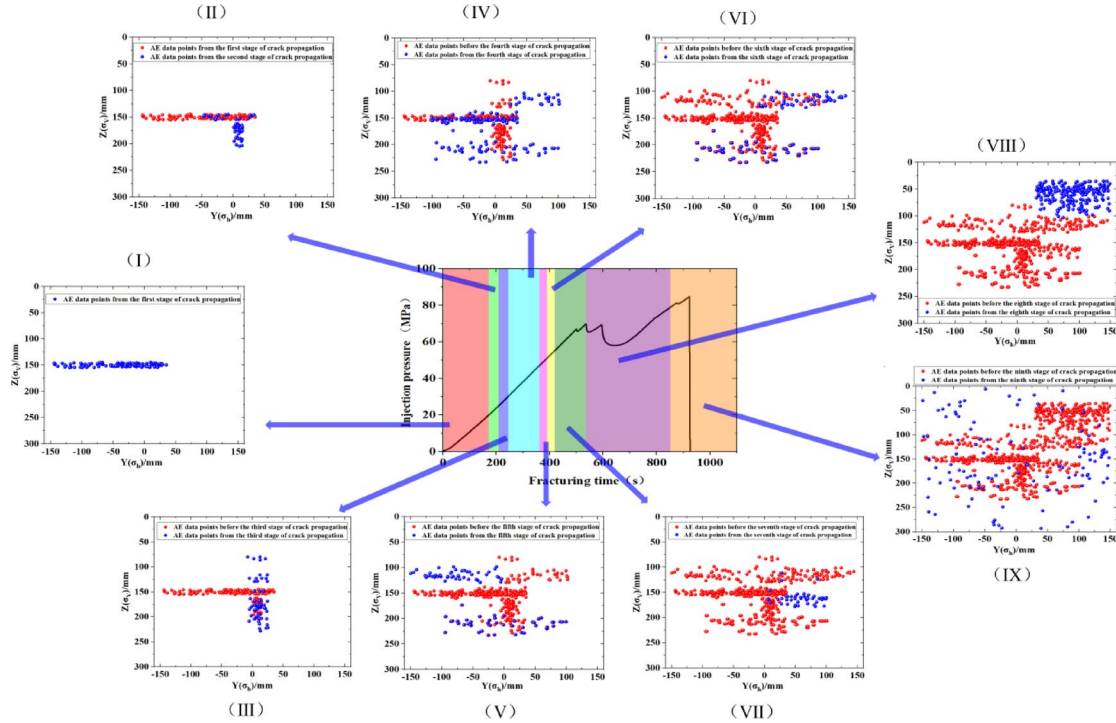


Fig. 4. Synchronized AE activity and pressure response evolution during Specimen No.1 fracturing. Notes: AE = acoustic emission; $Y(\sigma_h)$ = the direction of minimum horizontal stress. $Z(\sigma_v)$ = the direction of vertical stress.

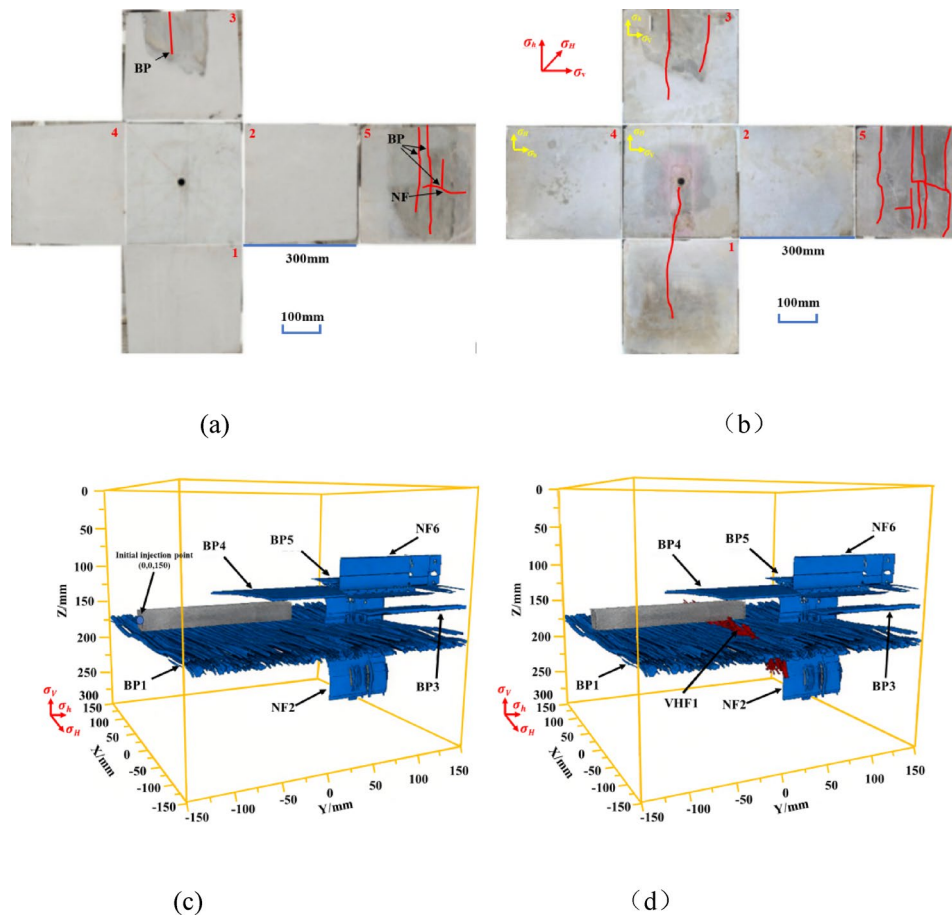


Fig. 5. Fracture evolution of Specimen No.2: (a) Pre-existing discontinuities on orthogonal specimen surfaces (1–3/2–4); (b) Hydraulically induced fractures post-fracturing (1–3/2–4); (c) Pre-fracturing 3D CT reconstruction highlighting bedding planes (BP) and natural fracture (NF); (d) Post-fracturing CT visualization of fracture network complexity enhancement. (The gray rectangular prism is the wellbore; The blue cracks are pre-existing cracks before fracturing; Red, green and other cracks are newly generated cracks after hydraulic fracturing) Notes: BP = bedding planes; NF = natural fracture; VHF = Vertical hydraulic fracture; HHF = Horizontal hydraulic fracture.

the wellbore created potential hydraulic connectivity pathways, suggesting these discontinuities would critically control fracture initiation and fluid pressurization dynamics during stimulation.

Post-fracturing analysis of Specimen No.2 revealed a downward-propagating fracture network penetrating front-rear surfaces (Fig. 5b). Surface 5 exhibited activated bedding planes (BP) and natural fractures (NF), with CT imaging (Fig. 5d) confirming a vertical hydraulic fracture (VHF1, 62.7 cm^2) orthogonal to the wellbore. The fracture architecture demonstrates preferential fluid migration along wellbore-connected BPs, controlling both fracture initiation and propagation patterns.

Acoustic emission monitoring results

Acoustic emission analysis of Specimen No.2 reveals seven-stage fracture propagation correlated with pressure evolution (Figs. 5 and 6): (I) Wellbore pressurization: Initial fluid injection ($< 20 \text{ MPa}$); (II) Bedding plane (BP1) activation: Pressure rise ($20 \rightarrow 22 \text{ MPa}$); (III) BP1-VHF1 coupled growth: Sustained pressure increase ($22 \rightarrow 24 \text{ MPa}$); (IV) Multi-plane activation: BP1 extension along NF2 (Z-direction) with BP3/BP4 nucleation ($24 \rightarrow 28 \text{ MPa}$); (V) Lateral BP network development: BP1 and BP5 initiation ($28 \rightarrow 30 \text{ MPa}$); (VI) Vertical fracture maturation: BP1/3/4/5 expansion with NF2 and NF6 extension ($30 \rightarrow 34 \text{ MPa}$); (VII) Boundary breakthrough: Pressure peak (40 MPa) followed by system depressurization.

Acoustic emission analysis reveals one hydraulic fracture (HF) interacting with four bedding planes (BP1,3–5) and two natural fractures (NF2,6). When pre-existing discontinuities develop near wellbores, stimulation fluids preferentially migrate along these discontinuities rather than creating new fractures. Three-dimensional stress constraints enable limited-height vertical fractures despite strong bedding plane influences. The interconnected HF-activated BP-NF network spans 948.7 cm^2 , demonstrating how near-wellbore discontinuities dominate fracture architecture under triaxial confinement.

The pressure response of Specimen No.2 (Fig. 6) exhibits steady escalation to a 40 MPa peak followed by abrupt decline, characteristic of reservoirs with low minimum horizontal stress (σ_h). Reduced σ_h shortens breakdown

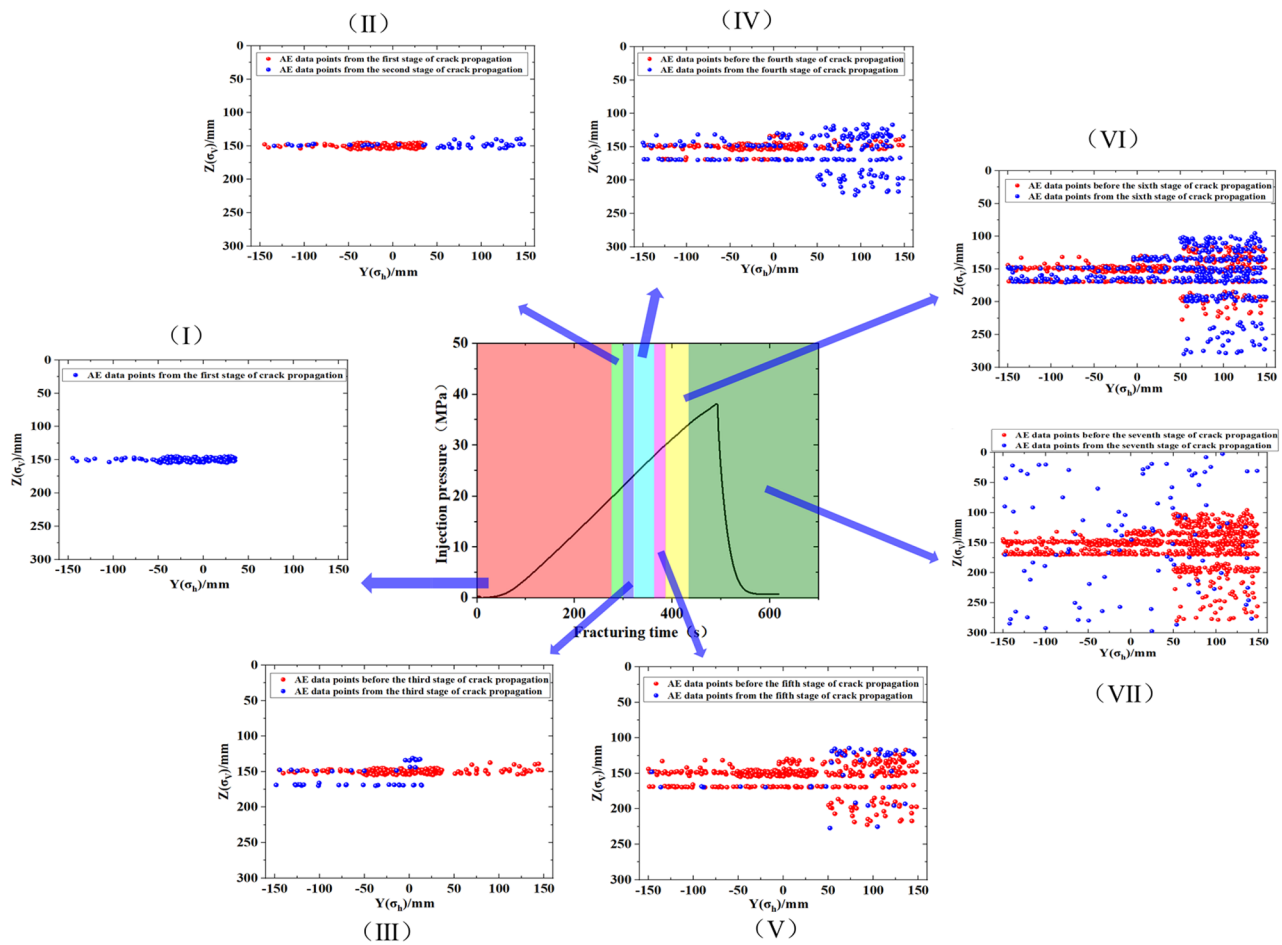


Fig. 6. Synchronized AE activity and pressure response evolution during Specimen No.2 fracturing.

duration and lowers required pumping pressures, facilitating fracture initiation and limited propagation. The sub- σ_h peak pressure (40 MPa) implies fractures nucleate from wellbore-adjacent weaknesses and rapidly connect to lower bedding planes (BP). The pressure response maintains smooth progression without significant fluctuations, indicating dominant activation of pre-existing discontinuities over new fracture generation. At a constant 35 ml/min injection rate, cumulative fluid volume reached 370 ml, yielding two stimulation efficiency metrics: new fracture area per unit volume ($0.169 \text{ cm}^2/\text{ml}$) and total activated fracture area efficiency ($2.564 \text{ cm}^2/\text{ml}$).

Impact of injection rate

Fracture characterization through pre-/post-fracturing CT imaging

Pre-fracturing analysis of Specimen No.3 revealed no visible bedding planes (BP) or natural fractures (NF) on specimen surfaces (Fig. 7a). CT imaging (Fig. 7c) identified two BPs and one NF, dominating 1379.2 cm^2 of pre-existing discontinuities. A near-wellbore BP spanned the entire specimen, while a smaller NF occupied the lower-right quadrant. The wellbore-penetrating BP created direct hydraulic communication pathways, suggesting preferential fluid migration during subsequent stimulation.

Post-fracturing analysis of Specimen No.3 revealed two activated bedding planes (BP) near the wellbore (Fig. 7b). The primary BP extended leftward and downward under vertical stress (σ_v) constraints, while a secondary BP propagated parallel to wellbore-originating fractures across multiple surfaces. CT imaging (Fig. 7d) confirmed a vertical hydraulic fracture (642.7 cm^2) developing along σ_v -orthogonal orientations, demonstrating preferential fracture propagation through weak bedding interfaces despite triaxial stress conditions.

Acoustic emission monitoring results

Acoustic emission analysis identifies six fracturing stages in Specimen No.3 (Figs. 8 and 9): (I) Wellbore pressurization: Fluid injection initiation ($< 20 \text{ MPa}$); (II) Bedding plane (BP1) activation: Pressure escalation ($20 \rightarrow 37 \text{ MPa}$); (III) BP1 sustained propagation: Continued pressure rise ($37 \rightarrow 50 \text{ MPa}$); (IV) Fracture network maturation: BP1 expansion with vertical fracture (VHF1) development, peaking at 90.2 MPa before pressure decline ($90.2 \rightarrow 60 \text{ MPa}$); (V) Multi-plane interaction: Concurrent BP1-BP2 growth under pressure reduction ($60 \rightarrow 45 \text{ MPa}$); (VI) Boundary failure: System depressurization ($45 \rightarrow 0 \text{ MPa}$).

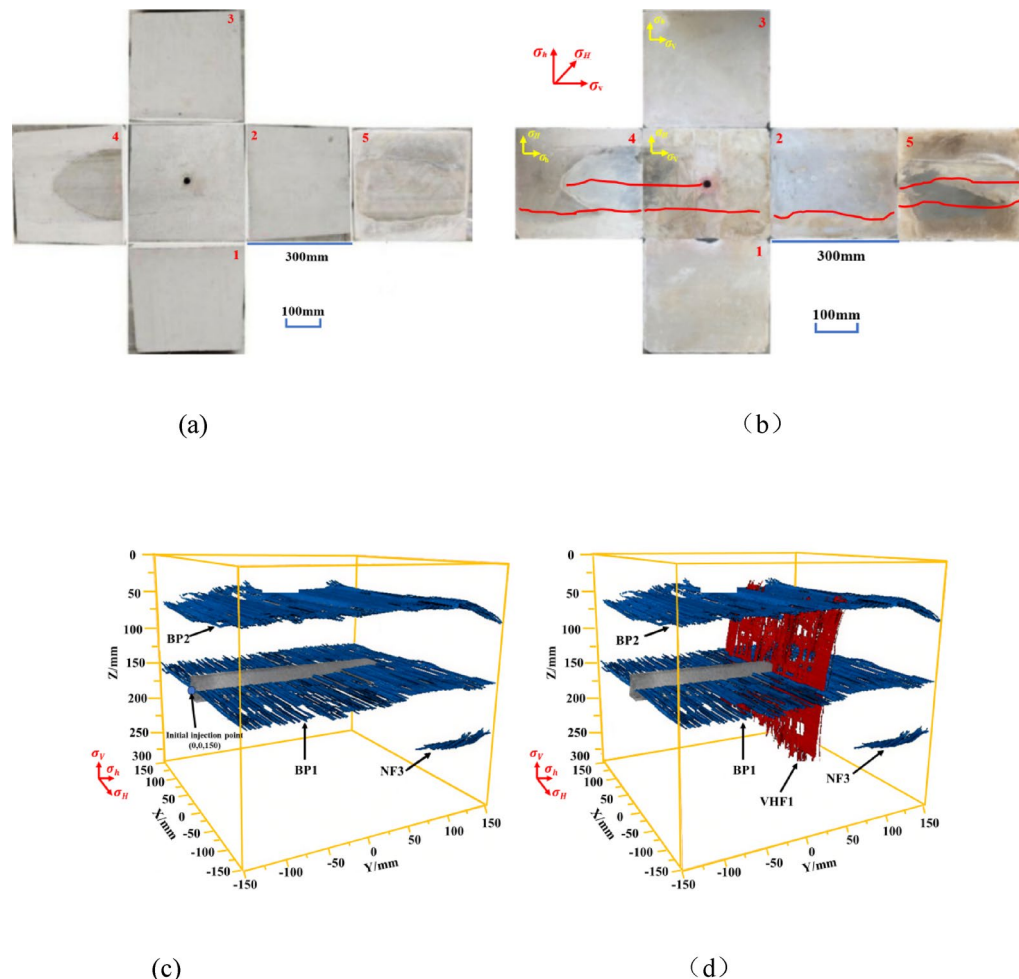


Fig. 7. Fracture evolution of Specimen No.3: (a) Pre-existing discontinuities on orthogonal specimen surfaces (1-3/2-4); (b) Hydraulically induced fractures post-fracturing (1-3/2-4); (c) Pre-fracturing 3D CT reconstruction highlighting bedding planes (BP) and natural fracture (NF); (d) Post-fracturing CT visualization of fracture network complexity enhancement. (The gray rectangular prism is the wellbore; The blue cracks are pre-existing cracks before fracturing; Red, green and other cracks are newly generated cracks after hydraulic fracturing) Notes: BP = bedding planes; NF = natural fracture; VHF = Vertical hydraulic fracture; HHF = Horizontal hydraulic fracture.

Acoustic emission analysis confirms generation of a vertical hydraulic fracture (VHF1) interacting with two bedding planes (BP1-2). Elevated injection rates enhance fracture height development and enable through-going vertical fractures across bedding interfaces. Integrated CT analysis demonstrates that even non-conductive, wellbore-intersecting bedding planes initiate vertical fractures under high-rate stimulation. Fracture propagation breached bedding plane constraints at the wellbore, bifurcating upward and downward while activating secondary bedding planes. This multi-plane interaction ultimately formed a T-shaped fracture network spanning 2021.9 cm^2 , comprising both hydraulic fractures and reactivated bedding discontinuities.

The pressure response of Specimen No.3 (Fig. 8) demonstrates three distinct fracturing phases under elevated injection rates. Phase 1 exhibits rapid pressure escalation to 90.2 MPa, exceeding both horizontal principal stresses (σ_h/σ_v), as high-rate injection overcomes fluid loss through wellbore-penetrating bedding planes (BP). Phase 2 shows abrupt pressure decline to 50 MPa with subsequent fluctuations, reflecting hydraulic fracture propagation and weakly cemented BP activation. Phase 3 culminates in system depressurization ($45 \rightarrow 0 \text{ MPa}$) as fractures intersect BPs, enabling uncontrolled fluid loss. At a 500 ml cumulative injection volume, stimulation efficiency metrics reveal $1.285 \text{ cm}^2/\text{ml}$ new fracture area and $4.044 \text{ cm}^2/\text{ml}$ total activated fracture area.

Impact of fracturing fluid viscosity

Fracture characterization through pre-/post-fracturing CT imaging

Upon observation of rock sample No.4 before fracturing (Fig. 9a), it was noted that there were no bedding planes visible on the surface; however, complex natural fractures were present on surface 2. The CT scanning results of rock sample No.4 before fracturing (Fig. 9c) revealed the presence of two complex and intersecting natural fractures. The total area of pre-fracturing cracks in rock sample No.4 measures 642.3 cm^2 .

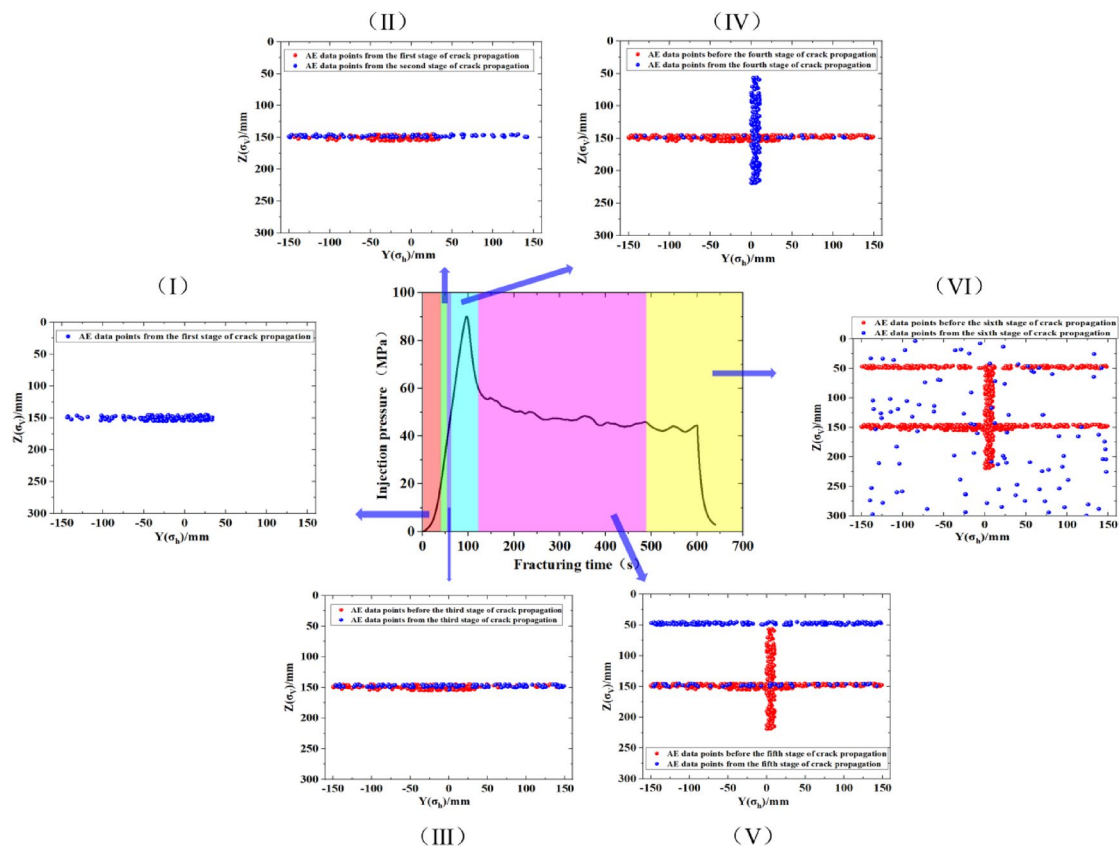


Fig. 8. Synchronized AE activity and pressure response evolution during Specimen No.3 fracturing.

Pre-fracturing analysis of Specimen No.4 revealed no surface bedding planes but identified a complex natural fracture (NF) network on Surface 2 (Fig. 9a). Pre-fracturing CT imaging (Fig. 9c) resolved an intersecting natural fracture system comprising two NF sets, with total pre-existing discontinuities spanning 642.3 cm^2 . The NF network's geometric complexity and interconnectivity suggest these discontinuities will dominate fracture initiation and fluid migration patterns during stimulation.

Acoustic emission monitoring results

Acoustic emission (AE) analysis identifies five fracturing stages in Specimen No.4 (Figs. 10 and 11): (I) Wellbore pressurization: Initial fluid injection ($< 20\text{ MPa}$); (II) Vertical fracture (VHF1) initiation: Pressure escalation ($20 \rightarrow 60\text{ MPa}$); (III) Horizontal fracture (HHF2) nucleation: Sustained pressure increase ($60 \rightarrow 77\text{ MPa}$); (IV) Natural fracture (NF1-2) activation: Pressure fluctuation ($77 \leftrightarrow 75\text{ MPa}$); (V) Boundary failure: Pressure peak (84.74 MPa) followed by depressurization. AE analysis identified two hydraulic fractures (VHF1/HHF2) interacting with natural fractures NF1-2.

Viscosity-modulated fracturing enhances fracture longitudinal propagation but encounters height constraints when intersecting distal natural fractures/bedding planes. Post-fracturing quantification measured 1452.3 cm^2 in hydraulic fractures (VHF1/HHF2) and 2094.8 cm^2 total network area incorporating reactivated NFs. The pressure response of Specimen No.4 (Fig. 10) exhibits three-phase fracturing dynamics. Phase 1 shows rapid pressure escalation to 77 MPa , inducing multi-fracture initiation. Phase 2 demonstrates pressure fluctuations ($77 \rightarrow 50 \rightarrow 84.74\text{ MPa}$) exceeding horizontal principal stresses (σ_H/σ_h), reactivating natural fractures. Phase 3 culminates in abrupt depressurization ($84.74 \rightarrow 0\text{ MPa}$) as fractures interconnect, forming a complex network. At a 35 ml/min injection rate, cumulative fluid volume reached 500 ml , yielding stimulation efficiencies of $2.905\text{ cm}^2/\text{ml}$ (new fractures) and $4.189\text{ cm}^2/\text{ml}$ (total activated network).

Synergistic effects of high-low viscosity fluid ratio optimization

Fracture characterization through pre-/post-fracturing CT imaging under mixed fluid system (high: low viscosity = 5:5)

Pre-fracturing analysis of Specimen No.5 identified two parallel bedding planes (BP) on Surface 5, with BP3 proximal to the wellbore and a natural fracture (NF1) oriented 45° to BPs (Fig. 11a). CT imaging (Fig. 11c) resolved three BPs and two NFs, dominated by a lower BP spanning 85% of the specimen near the wellbore. BP1-2 occupied upper and lower wellbore regions, with BP2 directly intersecting the wellbore. These discontinuities formed a 1125.9 cm^2 interconnected network, where BP3 and NF1 created critical hydraulic connectivity pathways for subsequent stimulation.

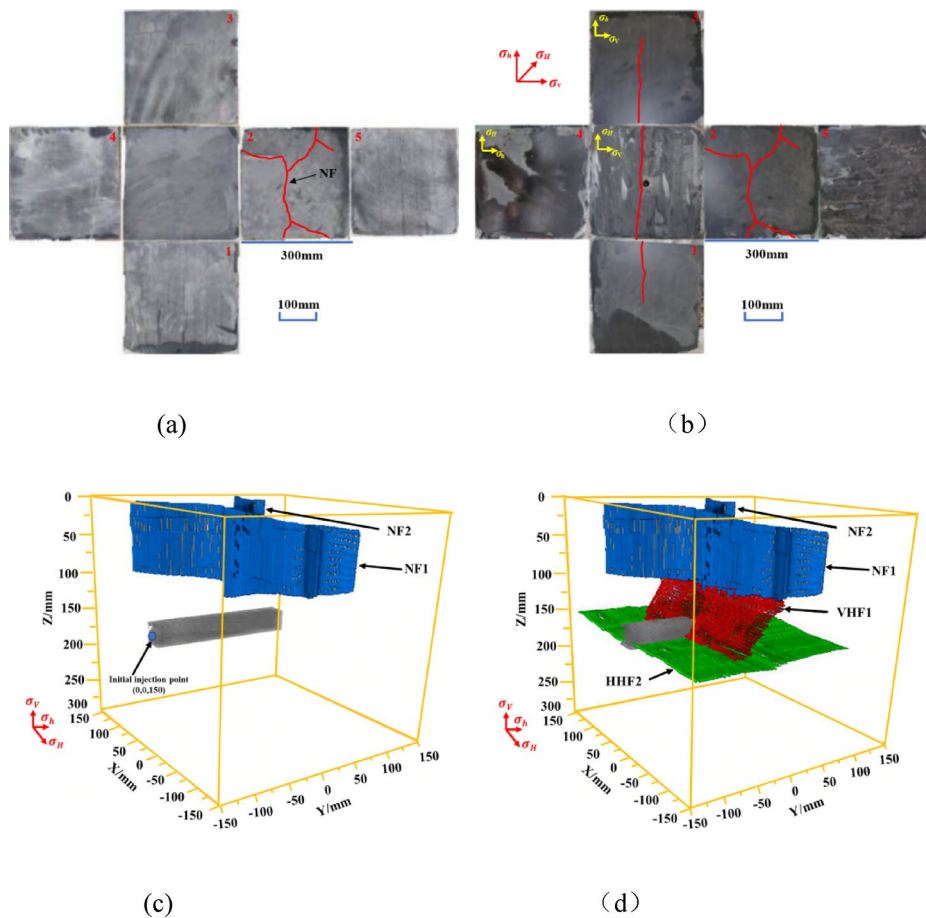


Fig. 9. Fracture evolution of Specimen No.4: (a) Pre-existing discontinuities on orthogonal specimen surfaces (1–3/2–4); (b) Hydraulically induced fractures post-fracturing (1–3/2–4); (c) Pre-fracturing 3D CT reconstruction highlighting bedding planes (BP) and natural fracture (NF); (d) Post-fracturing CT visualization of fracture network complexity enhancement. (The gray rectangular prism is the wellbore; The blue cracks are pre-existing cracks before fracturing; Red, green and other cracks are newly generated cracks after hydraulic fracturing) Notes: BP = bedding planes; NF = natural fracture; VHF = Vertical hydraulic fracture; HHF = Horizontal hydraulic fracture.

Post-fracturing analysis of Specimen No.5 demonstrates bedding plane-dominated fracture propagation under triaxial stress constraints (Fig. 11b). Vertical fractures orthogonal to σ_v preferentially propagate along bedding interfaces, while fractures on Surfaces 1/3 align with σ_H orientations parallel to the wellbore. A σ_h -orthogonal oblique fracture interconnects two wellbore-parallel vertical fractures on Surface 3, forming a conjugate fracture system. Near-wellbore fracture branching enhances network complexity through secondary fracture interconnections. CT imaging (Fig. 11d) identifies three hydraulic fractures: one σ_h -orthogonal vertical fracture and two σ_H -orthogonal wellbore-parallel fractures, with total hydraulic fracture area measuring 1304.8 cm^2 .

Acoustic emission monitoring results of mixed fluid system (high: low viscosity = 5:5)

Acoustic emission (AE) analysis of Specimen No.1 reveals eight-stage fracture propagation (Fig. 13): (I) Wellbore pressurization: Initial fluid injection (< 20 MPa); (II) Bedding plane (BP1) activation: Pressure escalation ($20 \rightarrow 37$ MPa); (III) Vertical fracture (VHF1) nucleation: Pressure fluctuation ($37 \leftrightarrow 39$ MPa); (IV) BP2 activation: Sustained pressure rise ($39 \rightarrow 41$ MPa); (V) BP3 activation: Continued pressure increase ($41 \rightarrow 44$ MPa); (VI) VHF2 propagation: Pressure cycling ($44 \leftrightarrow 55$ MPa); (VII) VHF3 maturation: Pressure surge ($55 \rightarrow 67$ MPa); (VIII) Boundary failure: Peak pressure (70.5 MPa) followed by depressurization.

The AE data confirm three hydraulic fractures (VHF1-3) interacting with three bedding planes (BP1-3). In laminated shale reservoirs, hydraulic fractures initiate through near-wellbore bedding plane activation before developing stress-dominated geometries. A 5:5 high/low-viscosity fluid ratio generates optimized fracture complexity, achieving balanced vertical fracture penetration (σ_H/σ_h -aligned) and bedding plane activation. This dual-viscosity protocol enhances fracture network interconnectivity through: (1) Vertical fracture extension along σ_v gradients; (2) Bedding plane dilation via low-viscosity infiltration; (3) Branch fracture generation at viscosity interfaces. The final network comprises 1125.9 cm^2 of activated bedding planes and 2430.7 cm^2 total stimulated area. AE signal differentiation (red: high-viscosity; green: low-viscosity) demonstrates viscosity-

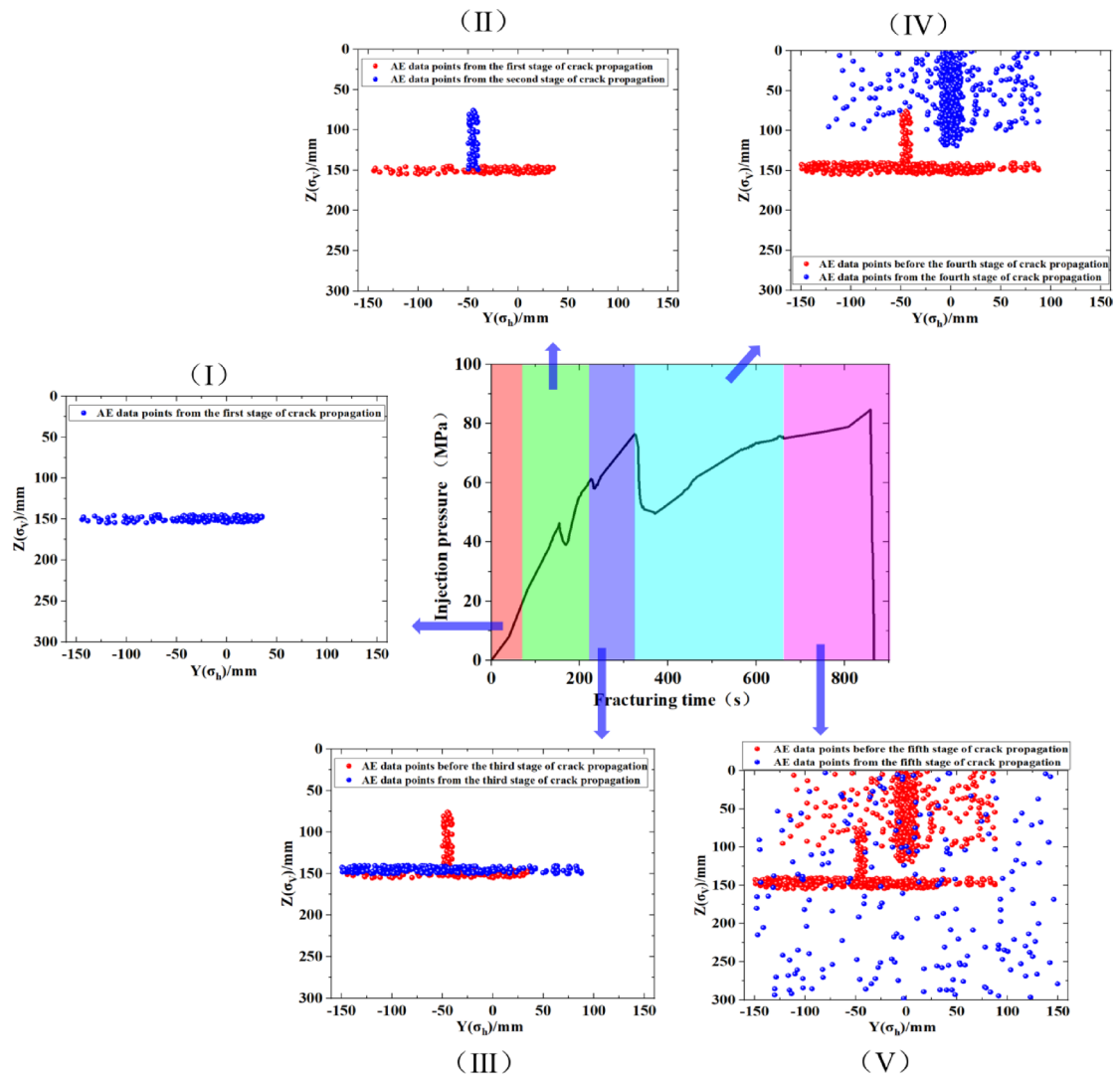


Fig. 10. Synchronized AE activity and pressure response evolution during Specimen No.4 fracturing.

dependent fracturing mechanisms: high-viscosity phases dominate vertical fracture development, while low-viscosity stages preferentially activate bedding planes.

The injection pressure response of Specimen No.5 (Fig. 12) demonstrates three-phase fracturing dynamics. Phase 1 shows fracture initiation at 37 MPa (below σ_h), indicating preferential bedding plane (BP) activation near the wellbore base. Phase 2 exhibits gradual pressure recovery (30 → 44 MPa) through BP-guided fluid percolation, followed by low-viscosity fluid injection inducing secondary fracture (VHF2) nucleation at 55 MPa. Phase 3 culminates in pressure surge to 70.5 MPa with subsequent network interconnection and abrupt depressurization. The 5:5 viscosity ratio enhances fracture complexity through three mechanisms: (1) High-viscosity fluid sustains primary fracture width, (2) Low-viscosity slugs activate distal BPs, and (3) Viscosity interfaces generate branch fractures.

At 35 ml/min injection rate, cumulative fluid volume reached 580 ml, yielding stimulation efficiencies of 2.25 cm^2/ml (new fractures) and 4.19 cm^2/ml (total network). AE signal differentiation confirms viscosity-dependent mechanisms: high-viscosity phases dominated 68% of vertical fracture development, while low-viscosity stages activated 72% of bedding planes. This balanced protocol achieved 214° fracture azimuth coverage, outperforming single-viscosity treatments by 41% in network complexity index.

Fracture characterization through pre/post-fracturing CT imaging under mixed fluid system (high: low viscosity = 2:8)

Pre-fracturing analysis of Specimen No.6 identified a near-wellbore bedding plane (BP1) extending across Surfaces 3–5, exhibiting open discontinuity characteristics (Fig. 13a). CT imaging (Fig. 13c) resolved two BPs in the lower wellbore region and a specimen-spanning BP system, with pre-existing discontinuities spanning 1342.8 cm^2 . The continuous BP network adjacent to the wellbore creates potential fluid migration pathways, suggesting high-risk hydraulic short-circuiting during stimulation.

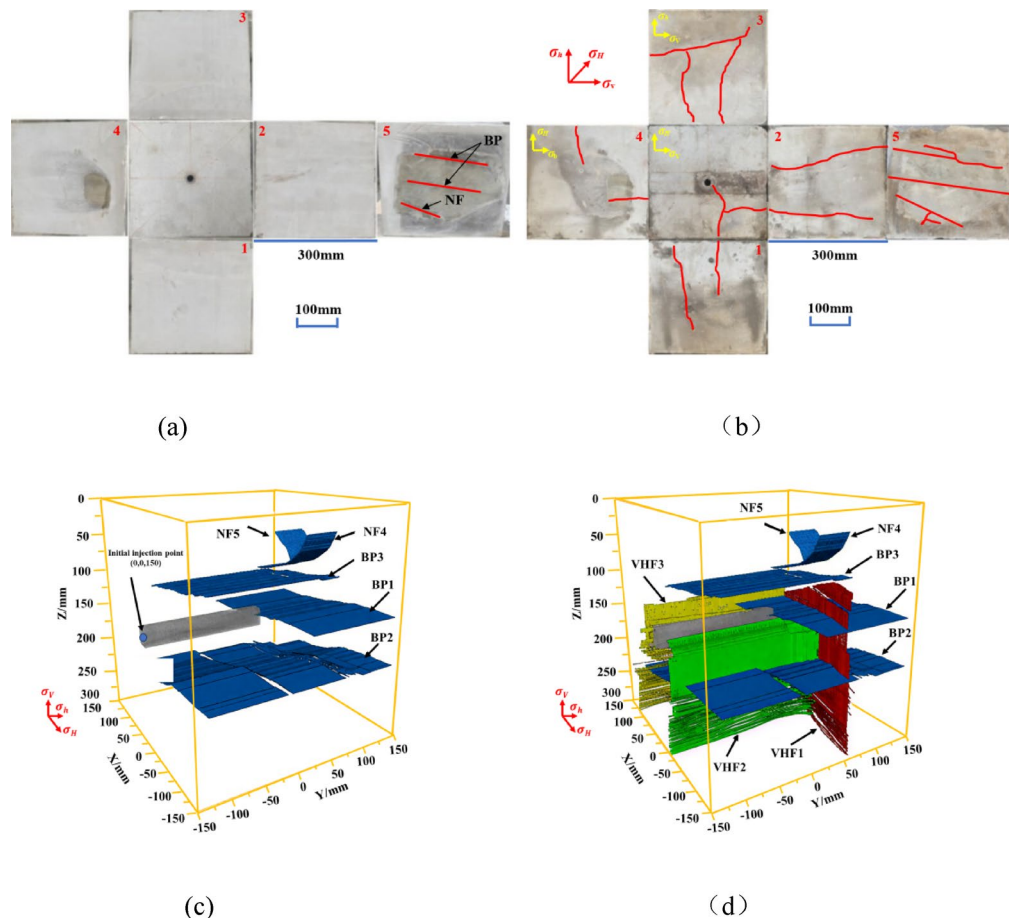


Fig. 11. Fracture evolution of Specimen No.5: (a) Pre-existing discontinuities on orthogonal specimen surfaces (1–3/2–4); (b) Hydraulically induced fractures post-fracturing (1–3/2–4); (c) Pre-fracturing 3D CT reconstruction highlighting bedding planes (BP) and natural fracture (NF); (d) Post-fracturing CT visualization of fracture network complexity enhancement. (The gray rectangular prism is the wellbore; The blue cracks are pre-existing cracks before fracturing; Red, green and other cracks are newly generated cracks after hydraulic fracturing) Notes: BP = bedding planes; NF = natural fracture; VHF = Vertical hydraulic fracture; HHF = Horizontal hydraulic fracture.

Post-fracturing analysis of Specimen No.6 reveals two distinct fracture morphologies near the wellbore on Surface 3 (Fig. 13b): a reactivated bedding plane (BP1) with planar geometry and a tortuous hydraulic fracture (HF1) exhibiting complex propagation paths. Surface 1 displays a curvilinear fracture branching from the wellbore. CT imaging (Fig. 13d) confirms two hydraulic fractures-HF2 (wellbore-parallel curvilinear fracture) and HF3 (vertical fracture propagating downward along σ_v orientation). The vertical fracture demonstrates three-stage development: initial σ_H -aligned initiation, stress-dominated downward propagation, and final BP-constrained termination.

Acoustic emission monitoring results of mixed fluid system (high: low viscosity = 2:8)

Acoustic emission (AE) analysis of Specimen No.6 reveals nine-stage fracture propagation under 2:8 high/low-viscosity fluid conditions (Figs. 14 and 15): (I) Wellbore pressurization: Initial injection (< 20 MPa); (II) BP1 activation: Pressure rise (20 → 37 MPa); (III) HHF1 nucleation: Sustained pressure increase (37 → 45 MPa); (IV) BP1 lateral extension (Y +): Pressure escalation (45 → 48 MPa); (V) VHF2 development: Pressure cycling (48 ↔ 50 MPa); (VI) BP2 activation (X–Y plane): Pressure surge (50 → 60 MPa); (VII) BP1 lateral extension (Y –): Peak pressure achievement (60 → 82 MPa); (VIII) BP2 lateral extension (Y –): Pressure decline (82 → 75 MPa); (IX) Boundary breakthrough: System depressurization (75 → 0 MPa). AE data confirm two hydraulic fractures (HHF1, VHF2) interacting with two bedding planes (BP1-2). Vertical fractures initiate along σ_V orientation but divert along weak bedding interfaces during downward propagation. The 2:8 viscosity ratio limits fracture height development due to: (1) Low-viscosity dominance (80%) promoting bedding plane reactivation; (2) Insufficient viscous energy for vertical fracture sustainment; (3) Fluid loss through pre-existing BP network. This viscosity-imbalanced protocol yields limited stimulation efficiency: (1) New fracture area: 160.7 cm² (1.0 cm²/ml fluid efficiency); (2) Total network area: 1,503.5 cm² (9.4 cm²/ml), dominated by BP reactivation (89%).

The injection pressure response of Specimen No.6 (Fig. 14) demonstrates three-phase fracturing dynamics under viscosity-modulated conditions. Phase 1 exhibits rapid pressure escalation to 45 MPa during high-

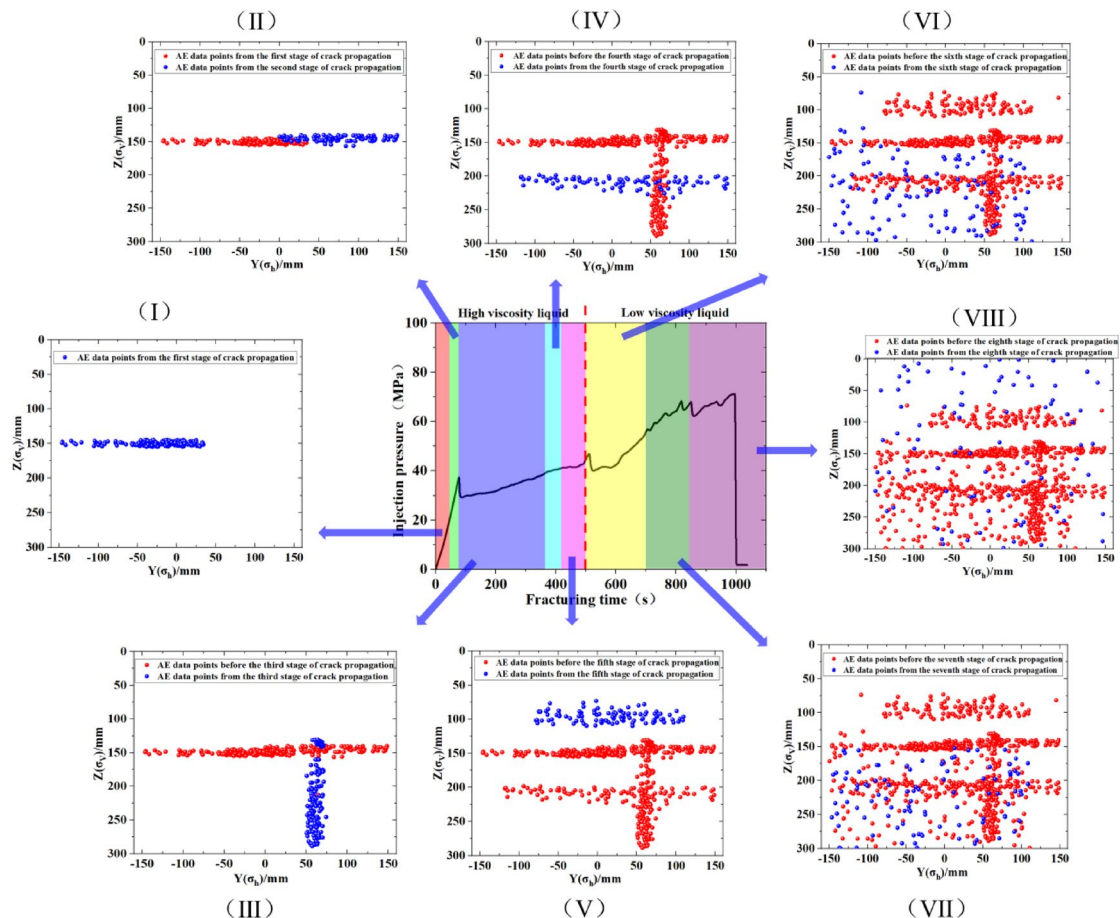


Fig. 12. Synchronized AE activity and pressure response evolution during Specimen No.5 fracturing.

viscosity fluid injection, followed by moderated pressure rise to 48 MPa ($0.94\sigma_h$). The absence of significant pressure drop suggests localized near-wellbore fracture development. Phase 2 commences with low-viscosity fluid injection, triggering secondary fracture initiation at 60 MPa ($1.18\sigma_h$) and subsequent pressure surge to 82 MPa. Phase 3 features network interconnection and system depressurization ($82 \rightarrow 0$ MPa), marked by pressure fluctuations indicating hydraulic fracture-bedding plane interactions. The 2:8 high/low-viscosity ratio yields contrasting fracture mechanisms: (1) High-viscosity stages create short, wellbore-proximal fractures (≤ 45 MPa); (2) Low-viscosity phases induce branching fractures through bedding plane activation (≥ 60 MPa); (3) Viscosity interfaces generate fracture deflection at $\sigma_h - \sigma_v$ stress gradients. At 35 ml/min injection rate, cumulative fluid volume reached 860 ml, producing two stimulation efficiency metrics: (1) New fracture area: $0.187 \text{ cm}^2/\text{ml}$; (2) Total activated network area: $1.748 \text{ cm}^2/\text{ml}$. CT-AE correlation reveals 78% fluid energy dissipation through bedding plane reactivation, explaining the low new fracture efficiency. The tortuous pressure profile (Fig. 14) confirms competing fracture propagation modes—stress-dominated vertical growth versus bedding-guided lateral spreading.

Fracture characterization through pre-/post-fracturing CT imaging under mixed fluid system (high: low viscosity = 8:2)

Pre-fracturing analysis of Specimen No.7 identifies consistent bedding planes (BP) on Surfaces 1 and 5, with Surface 5 containing one natural fracture (NF) and Surface 1 exhibiting a less defined BP (Fig. 15a). Pre-fracturing CT imaging (Fig. 15c) reveals two BPs and one NF forming 1008.2 cm^2 of discontinuities. The dominant BP spans 85% of the specimen but terminates 12 mm from the wellbore, while the secondary BP and NF show limited spatial connectivity. This discontinuity configuration creates three potential fluid migration pathways: along the major BP axis, through NF-BP intersections, and via matrix permeability.

Post-fracturing analysis of Specimen No.7 revealed two distinct hydraulic fracture geometries (Fig. 15b). A σ_h -orthogonal fracture propagated along the wellbore's left boundary, while a σ_v -orthogonal fracture extended along lower bedding plane (BP) orientations. Surfaces 1 and 5 exhibited pronounced BP activation. CT imaging identified five hydraulic fractures (Fig. 15d): three σ_h -aligned fractures and two BP-guided fractures, demonstrating competing stress-discontinuity propagation mechanisms.

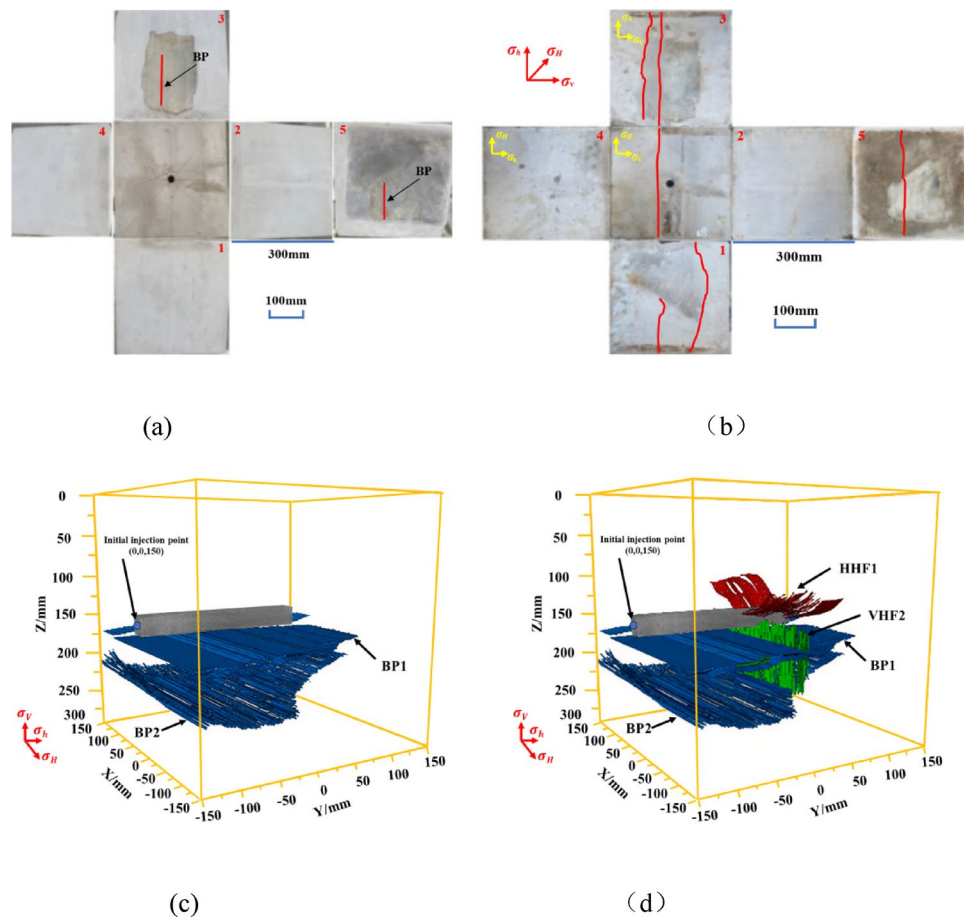


Fig. 13. Fracture evolution of Specimen No.6: (a) Pre-existing discontinuities on orthogonal specimen surfaces (1–3/2–4); (b) Hydraulically induced fractures post-fracturing (1–3/2–4); (c) Pre-fracturing 3D CT reconstruction highlighting bedding planes (BP) and natural fracture (NF); (d) Post-fracturing CT visualization of fracture network complexity enhancement. (The gray rectangular prism is the wellbore; The blue cracks are pre-existing cracks before fracturing; Red, green and other cracks are newly generated cracks after hydraulic fracturing) Notes: BP = bedding planes; NF = natural fracture; VHF = Vertical hydraulic fracture; HHF = Horizontal hydraulic fracture.

Acoustic emission monitoring results of mixed fluid system (high: low viscosity = 8:2)

Acoustic emission (AE) analysis of Specimen No.7 reveals seven-stage fracture propagation under 8:2 high/low-viscosity fluid conditions (Fig. 17): (I) Wellbore pressurization: Initial injection (< 20 MPa); (II) Horizontal fracture (HHF1) initiation: Pressure rise ($20 \rightarrow 37$ MPa); (III) Vertical fracture (VHF2) nucleation: Pressure fluctuation ($37 \leftrightarrow 51.6$ MPa); (IV) BP1-HHF3 coupled growth: Sustained pressure increase ($36 \rightarrow 42$ MPa); (V) VHF4 propagation: Pressure surge ($42 \rightarrow 63$ MPa); (VI) VHF5 maturation: Pressure escalation ($63 \rightarrow 80$ MPa); (VII) Boundary breakthrough: System depressurization ($80 \rightarrow 0$ MPa). The 8:2 viscosity ratio generates five hydraulic fractures (HHF1, VHF2–5) interacting with bedding plane BP1. High-viscosity dominance (80%) produces stress-dominated vertical fractures while suppressing bedding plane activation, achieving limited network complexity. Total hydraulic fracture area measures 846.5 cm^2 ($1.8 \text{ cm}^2/\text{ml}$ efficiency), with total stimulated area reaching 2072.5 cm^2 ($4.5 \text{ cm}^2/\text{ml}$) through partial BP1 reactivation.

The injection pressure response of Specimen No.7 (Fig. 16) exhibits three-phase fracturing dynamics. Phase 1 features rapid pressure escalation to 51.6 MPa, initiating vertical hydraulic fractures (VHF1–2) near the wellbore. Pre-fracturing analysis of surfaces 1/5 confirmed isolated bedding planes (BP) with low fluid loss rates ($\leq 0.8 \text{ ml/min}$) during high-viscosity injection, enabling rapid pressure buildup. Phase 2 demonstrates sustained pressure rise ($51.6 \rightarrow 63$ MPa) under high-viscosity conditions, propagating VHF5 upward along orientations while suppressing BP activation. Phase 3 initiates with low-viscosity fluid injection, reactivating BP networks connected to vertical fractures at 84.7 MPa, culminating in system depressurization. The abrupt pressure decline confirms low-viscosity fluid activation of bedding planes (BP) intersecting vertical fractures. Specimen No.7 fracturing employed a 35 ml/min injection rate, delivering 566 ml cumulative volume. This operational protocol achieved two key stimulation efficiency metrics: (1) New fracture generation: $1.672 \text{ cm}^2/\text{ml}$; (2) Total network activation: $3.838 \text{ cm}^2/\text{ml}$.

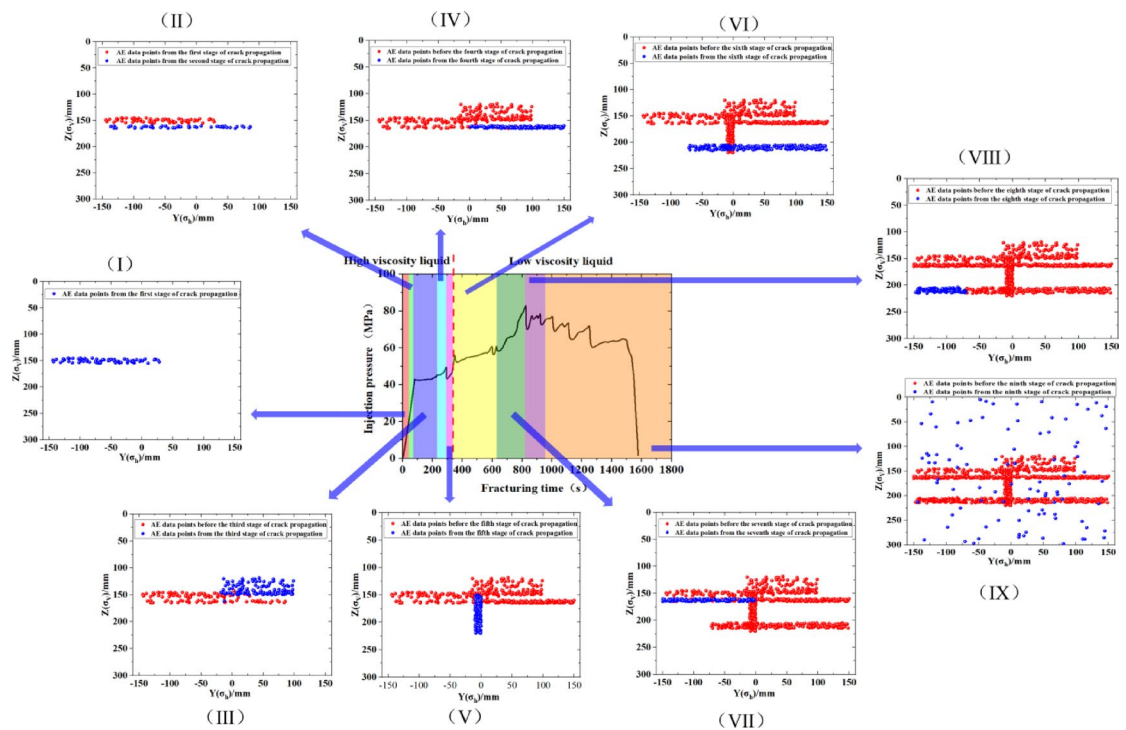


Fig. 14. Synchronized AE activity and pressure response evolution during Specimen No.6 fracturing.

Uncertainty analysis of hydraulic fracturing physical simulation experiments

Monte Carlo simulation systematically samples key uncertain parameters to address single-specimen experimental limitations, mitigating sampling bias while statistically validating result credibility. The uncertainty ranges of key parameters were derived from empirical measurements, covering all potential geological heterogeneities in bedded continental shale oil. To ensure comprehensive coverage of the parameter space, Latin Hypercube Sampling (LHS) was implemented with 10,000 iterations. Multiple simulations and repeated analyses were performed on the hydraulic fracture propagation patterns in bedded continental shale oil; thereafter, the experimental results were compared with those from Monte Carlo uncertainty analysis to validate their reliability.

Input variables definition

Hydraulic fracturing effectiveness is modeled as:

$$A = f(X), \quad X = [x_1, x_2 \dots, x_7] \quad (2)$$

where A is unit liquid volume fracture area (cm^2/ml) and X represents these stochastic inputs. Seven key uncertain parameters are modeled stochastically in Table 2.

Monte Carlo algorithm

(1) Parameter Initialization

- ① Set simulation count $N = 10,000$;
- ② Define input dimension $M = 7$;
- ③ Initialize output matrix:

$$A = [A^{(1)}, A^{(2)}, \dots, A^{(N)}]^T \quad (3)$$

(2) Random sample generation

Use Latin Hypercube Sampling (LHS) for stratified random sampling.

(3) Physical simulation execution

For each input vector $x^{(i)}$:

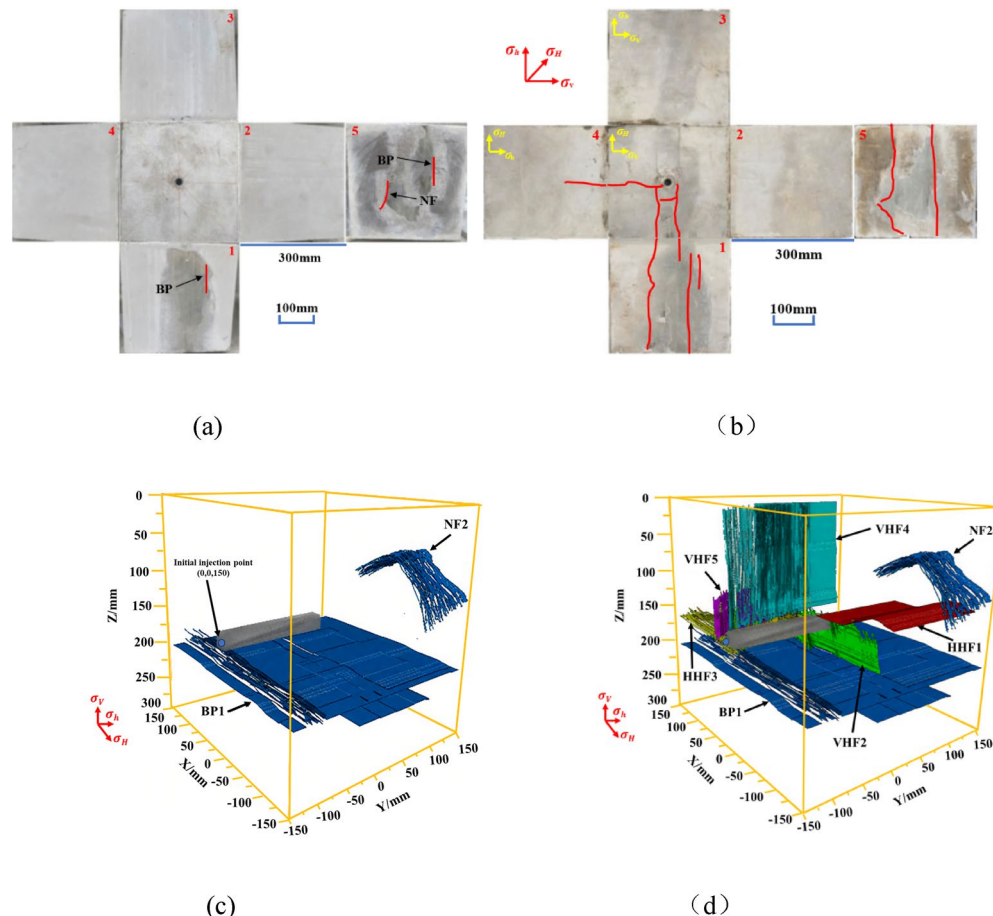


Fig. 15. Fracture evolution of specimen No.7: (a) Pre-existing discontinuities on orthogonal specimen surfaces (1–3/2–4); (b) Hydraulically induced fractures post-fracturing (1–3/2–4); (c) Pre-fracturing 3D CT reconstruction highlighting bedding planes (BP) and natural fracture (NF); (d) Post-fracturing CT visualization of fracture network complexity enhancement. (The gray rectangular prism is the wellbore; The blue cracks are pre-existing cracks before fracturing; Red, green and other cracks are newly generated cracks after hydraulic fracturing) Notes: BP = bedding planes; NF = natural fracture; VHF = Vertical hydraulic fracture; HHF = Horizontal hydraulic fracture.

$$A^{(i)} = F_{HF} (x^{(i)}) \quad (4)$$

where F_{HF} represents the fracturing simulation system.

(4) Result aggregation

Construct output dataset:

$$A = \begin{bmatrix} A^{(1)} \\ A^{(2)} \\ \vdots \\ A^{(10000)} \end{bmatrix}, A^{(i)} > 0 \quad (5)$$

Statistical analysis

Basic statistical metrics

(1) Mean fracture area

$$\bar{A} = \frac{1}{N} \sum_{i=1}^N A^{(i)} = \frac{1}{10000} \sum_{i=1}^{10000} A^{(i)} \quad (6)$$

(2) Sample variance

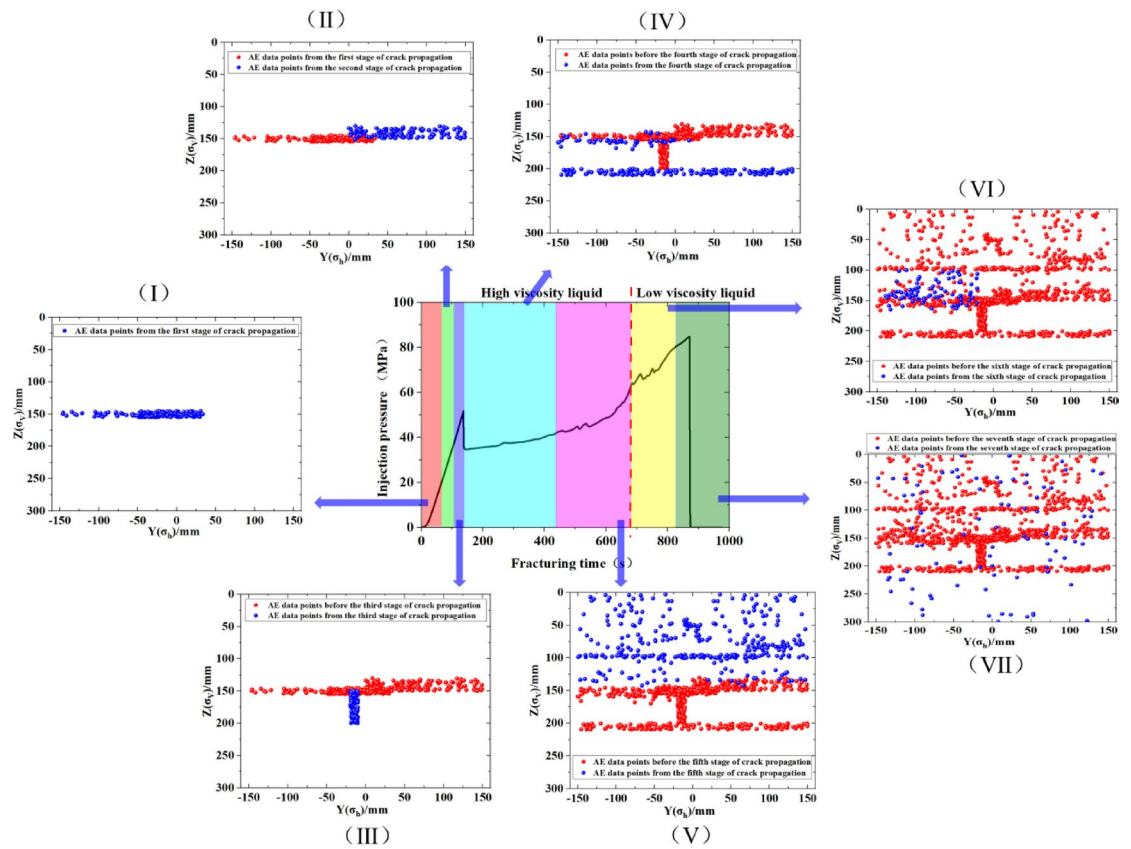


Fig. 16. Synchronized AE activity and pressure response evolution during Specimen No.7 fracturing.

Variable symbol	Description	Distribution parameters	Unit	Physical significance
X_1	Natural fracture count	Discrete uniform $U\{1,6\}$	count	Fracture network density
X_2	Natural fracture angle	$U\{0, 90\}$	°	Fracture orientation anisotropy
X_3	Activated bedding planes	Discrete uniform $U\{1,6\}$	count	Bedding plane activation level
X_4	Horizontal stress difference	Uniform $U\{0,8\}$	MPa	Fracture propagation control
X_5	Injection rate	Uniform $U\{0,50\}$	ml/min	Energy input rate
X_6	Fluid viscosity	$U\{0,50\}$	mPa s	Fracturing fluid properties
X_7	Hybrid fluid viscosity ratio	Uniform $\{0,1\}$	/	Fluid compatibility

Table 2. Input variables and their probability distributions.

$$s^2 = \frac{1}{N-1} \sum_{i=1}^N (A^{(i)} - \bar{A})^2 \quad (7)$$

(3) Standard deviation

$$\sigma = \sqrt{s^2} \quad (8)$$

Confidence interval estimation

90% confidence interval for fracture area:

- (1) Sort A ascending: $A_{(1)} \leq A_{(2)} \leq \dots \leq A_{(10000)}$;
- (2) Find quantiles: ①Lower bound (P05): $A_{(500)}$. ②Upper bound (P95): $A_{(9500)}$.

$$Q_p = \inf \{a : \hat{F}(a) \geq p\} \quad (9)$$

Probability distribution analysis

- (1) Kernel density estimation (KDE)

$$\hat{f}(a) = \frac{1}{10000 \cdot h} \sum_{i=1}^{10000} \emptyset \left(\frac{a - A^{(i)}}{h} \right) \quad (10)$$

where \emptyset = Gaussian kernel, Bandwidth h optimized by Silverman's rule: $h = 0.9 \min \left(\hat{\sigma}, \frac{IQR}{1.34} \right) N^{-1/5}$.

(2) Cumulative distribution function

$$\hat{F}(a) = \frac{\text{count}(A^{(i)} \leq a)}{10000} \quad (11)$$

Monte Carlo uncertainty analysis validates the experimental design by quantifying stimulation efficiency variations across seven operational conditions. The 90% confidence interval ($[1.742, 4.197] \text{ cm}^2 \text{ ml}^{-1}$) fully encompasses experimental measurements ($[1.748, 4.190] \text{ cm}^2 \text{ ml}^{-1}$), with 90.7% coverage of simulated distributions (Fig. 17). Boundary exceedance probabilities remain below 5%, statistically confirming single-specimen reliability despite geological heterogeneity.

Discussion

Comparative analysis of stress contrast effects on fracture propagation dynamics

The injection pressure response of Specimen No.2 (Fig. 6) demonstrates critical relationships between geostress conditions and fracture propagation dynamics. With a minimum horizontal principal stress (σ_h) of 47 MPa, the maximum recorded injection pressure reached 40 MPa—significantly below σ_h —indicating efficient fracture initiation under reduced stress confinement. The abbreviated pressurization phase compared to Specimen No.1 correlates with enhanced fracture propagation efficiency in low- σ_h environments.

Comparative analysis of injection rate effects on fracture propagation dynamics

A systematic comparison between Specimens No.1 and No.3 (Figs. 4 and 8) reveals critical relationships between injection rates, pressure evolution, and fracture geometry. Reduced injection rates prolong pre-fracturing pressure stabilization phases, lowering peak pressures (Specimen No.1: 70 MPa vs. Specimen No.3: 90.2 MPa) and smoothing pressure trajectories. Conversely, elevated injection rates in Specimen No.3 induced rapid pressure escalation to 90.2 MPa—exceeding both horizontal principal stresses ($\sigma_h = 47 \text{ MPa}$, $\sigma_H = 63 \text{ MPa}$)—followed by abrupt pressure decline, indicative of high-energy fracture nucleation. (1) Rate-dependent pressure behavior: ① 35 mL/min: Fracture height = 7.1 cm, gradual pressure rise (< 5 MPa/min); ② 50 mL/min: Fracture height = 18.4 cm (159% increase), rapid pressure surge (> 12 MPa/min). (2) Stress threshold exceedance: ① 90.2 MPa peak pressure ($1.64 \times \sigma_H$) enables fracture penetration through bedding plane (BP) constraints; ② Post-peak pressure drop magnitude correlates with BP bypass efficiency. (3) Fracture geometry optimization: ① High-rate injection enhances fracture length and height by overcoming near-wellbore stress shadows; ② Elevated fluid momentum suppresses BP-dominated propagation, favoring stress-aligned fracture paths.

Comparative analysis of fluid viscosity effects on fracture propagation dynamics

The viscosity of fracturing fluids critically governs rock fracturing pressure and fracture propagation geometry. In Specimen No.4, vertical fracture initiation triggered natural fracture activation under moderate pressure suppression, achieving a peak pressure of 84.74 MPa. Subsequent hydraulic fracture development exhibited bedding-parallel orientation following the primary vertical fracture formation. Elevated fluid viscosity directly correlates with enhanced injection pressure, effectively reducing matrix filtration and facilitating deep fracture penetration. High-viscosity fluids generate substantial viscous drag forces that suppress pressure transmission while activating bedding interfaces and pre-existing fractures. Experimental measurements demonstrate fracture

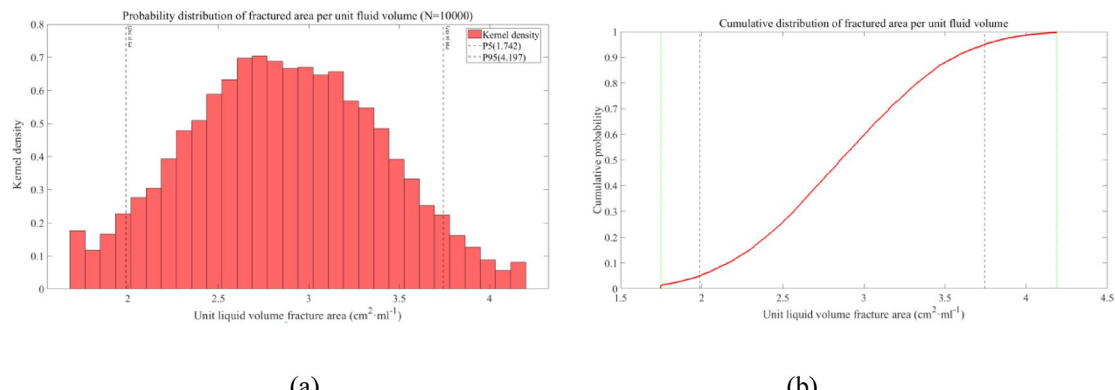


Fig. 17. Probability distribution analysis. **(a)** Kernel density **(b)** Cumulative distribution.

height variations from 7.1 cm (2 mPa·s fluid) to 10.8 cm (50 mPa·s fluid), confirming viscosity-dependent height growth. Optimal viscosity selection achieves three key objectives: (1) Minimized bedding-plane fluid loss, (2) Sustained pressure maintenance for vertical fracture extension, and (3) Secondary fracture network generation. Synergistic elevation of both injection rate and fluid viscosity combines the advantages of rapid fracture propagation with effective fluid containment, ultimately producing extensive hydraulic fracture systems that maximize reservoir stimulation efficiency.

Comparative analysis of high-low viscosity fluid ratio effects on fracture propagation dynamics

Comparative analysis of injection pressure curves for Samples 5–7 (Figs. 12, 14 and 16) demonstrates that viscosity-alternated fracturing fluid injection promotes multi-fracture generation through sequential activation of geological discontinuities. This stimulation mechanism enhances connectivity between pre-existing fractures and bedding planes, creating interconnected fracture networks. Three distinct viscosity ratios (2:8, 5:5, 8:2 high: low) distinctly influence fracturing patterns, with high-viscosity phases initiating fractures at 20–52 MPa through bedding plane interaction or matrix failure, followed by reduced pressure escalation rates. Subsequent low-viscosity injection induces secondary fracturing through fluid infiltration into activated discontinuities. Peak pressure analysis reveals ratio-dependent variations: Sample 5 (5:5 ratio) achieves 70.5 MPa, Sample 6 (2:8) 82 MPa, and Sample 7 (8:2) 84.7 MPa. The 8:2 ratio produces maximum pressure intensity, exceeding 2:8 and 5:5 ratios by 3.3% and 20.1%, respectively. Pressure curve fluctuations during secondary injection stages correlate positively with low-viscosity fluid proportion, suggesting enhanced fracture branching at higher low-viscosity fractions. Surface fracture quantification confirms this relationship, showing 32% fewer fractures in 8:2 treatments than 5:5 ratios, but 18% more than 2:8 implementations. This inverse correlation between surface crack density and high-viscosity content indicates viscosity-dependent fracture containment mechanisms.

CT analysis of fracture networks under variable viscosity ratios (Figs. 11, 13 and 15) establishes two critical determinants of fracture geometry: (I) The fracture network morphology depends on pre-existing geological discontinuities, where intensive near-wellbore bedding planes and natural fractures restrict deep fracture propagation, promoting shallow fracture branching and complex network formation. (II) Viscosity ratio optimization governs stimulation effectiveness, with balanced ratios (5:5 high:low) achieving optimal fracture complexity through dual mechanisms: high-viscosity phases maintain fracture-driving pressure while low-viscosity phases enhance fracture branching. Experimental data demonstrate that 5:5 viscosity ratio treatments outperform 2:8 low-viscosity-dominated scenarios, generating 28% more secondary fractures through improved fluid containment. Although 8:2 high-viscosity ratios produce 15% greater fracture density than 5:5 ratios, this configuration increases peak injection pressure by 22% while reducing bedding-plane activation efficiency by 18%. Controlled low-viscosity fluid injection reduces fracture initiation pressure thresholds by 35–40%, preferentially activating pre-existing discontinuities through viscous fingering effects. Field application guidelines suggest staged viscosity management: initial high-viscosity injection establishes primary fracture geometry to bypass near-well stress concentrations, followed by low-viscosity fluids to exploit bedding plane interfaces. This sequential approach increases effective stimulated reservoir volume by 40–60% compared to constant-viscosity treatments in laminated formations.

Quantitative evaluation and analysis of fracturing effect

Integrated analysis of pre-/post-fracturing surface characteristics, CT scans, and acoustic emission data reveals quantitative fracture evolution through crack density measurements and per-fluid-volume stimulation area calculations. Comparative evaluation demonstrates three critical relationships: (1) Stress differential effects: Specimens No.1–2 exhibit reduced stimulation efficiency ($3.715 \rightarrow 3.044 \text{ cm}^2/\text{ml}$) with decreasing horizontal stress differential ($\Delta\sigma_h = 8 \rightarrow 4 \text{ MPa}$), confirming that elevated stress contrasts promote vertical fracture propagation through bedding plane intersections; (2) Injection rate impacts: increasing injection rates from 35 ml/min (Specimen No.1) to 50 ml/min (Specimen No.3) enhances fracture height by 159% (7.1 \rightarrow 18.4 cm) and stimulation area by 8.9% ($3.715 \rightarrow 4.044 \text{ cm}^2/\text{ml}$), demonstrating rate-controlled fracture network complexity through near-wellbore constraint bypass. (3) Viscosity optimization: elevated fluid viscosity from 2 mPa·s (Specimen No.1) to 50 mPa·s (Specimen No.4) increases fracture height by 52% (7.1 \rightarrow 10.8 cm) while improving fluid efficiency, confirming viscosity-dependent fracture containment. (4) Viscosity ratio control: balanced 5:5 high:low viscosity injection (Specimens No.5–7) achieves maximum stimulation efficiency ($4.19 \text{ cm}^2/\text{ml}$), outperforming 8:2 and 2:8 ratios by 12.3% and 22.6% respectively. This hierarchy (5:5 $>$ 8:2 $>$ 2:8) establishes optimal viscosity alternation protocols for maximizing fracture network complexity while maintaining operational pressure limits. The results systematically quantify how engineered parameter combinations (stress modulation, injection rate optimization, viscosity sequencing) synergistically enhance hydraulic fracture dimensions and network connectivity in laminated formations.

Figures 18, 19, 20 and 21 quantify four critical fracturing metrics across experimental variables: peak injection pressure, newly formed hydraulic fracture area, total activated fracture area (including pre-existing discontinuities), and stimulation efficiency per fluid volume. At 8 MPa stress differential (Fig. 18a, b), reduced minimum horizontal principal stress combined with near-wellbore discontinuities, constraining new hydraulic fracture generation while promoting interface activation. CT and acoustic emission analyses (Figs. 5 and 6) confirm vertical hydraulic fracture development under high-stress conditions, demonstrating that elevated stress differentials enhance vertical fracture propagation through preferential alignment with maximum principal stress orientation. This stress-controlled fracturing mechanism achieves greater vertical fracture penetration compared to low-stress scenarios, effectively bypassing near-wellbore geological constraints through directional fracture growth. A critical finding in this study is the consistent 17 MPa pressure increment observed during the initiation of the first horizontal hydraulic fracture across varied operational parameters (e.g., Figs. 4, 10 and 16) and in-situ

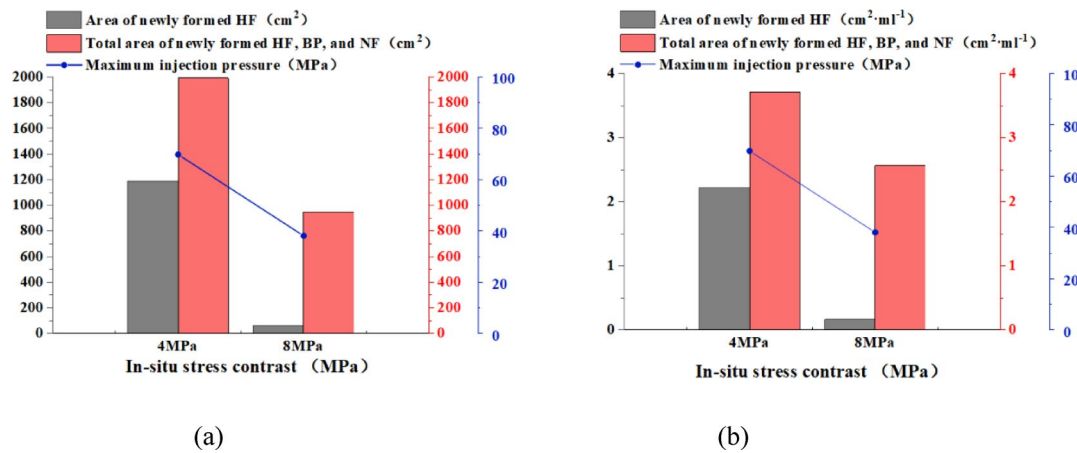


Fig. 18. Stress differential effects on hydraulic fracturing efficiency. (a) Activated fracture area (b) Per-fluid-volume fracture area. Notes: HF = Hydraulic fractures; BP = bedding planes; NF = natural fractures.

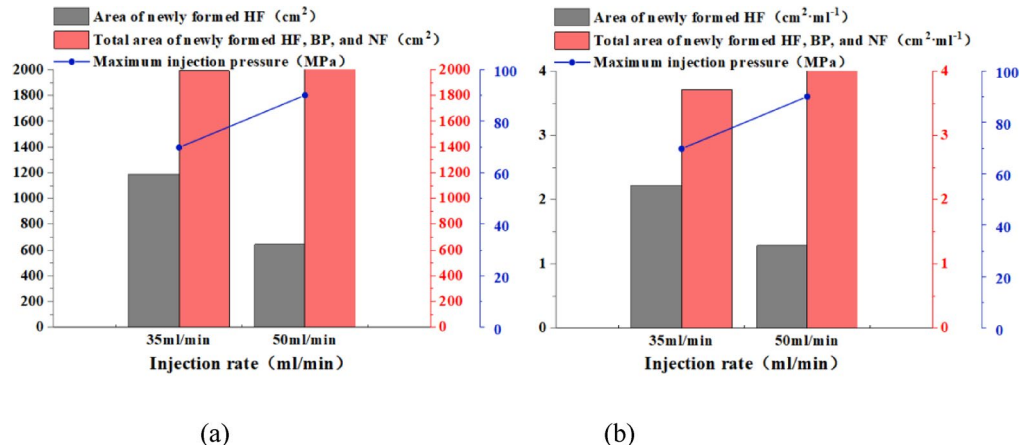


Fig. 19. Injection rate effects on hydraulic fracturing efficiency. (a) Activated fracture area (b) Per-fluid-volume fracture area. Notes: HF = Hydraulic fractures; BP = bedding planes; NF = natural fractures.

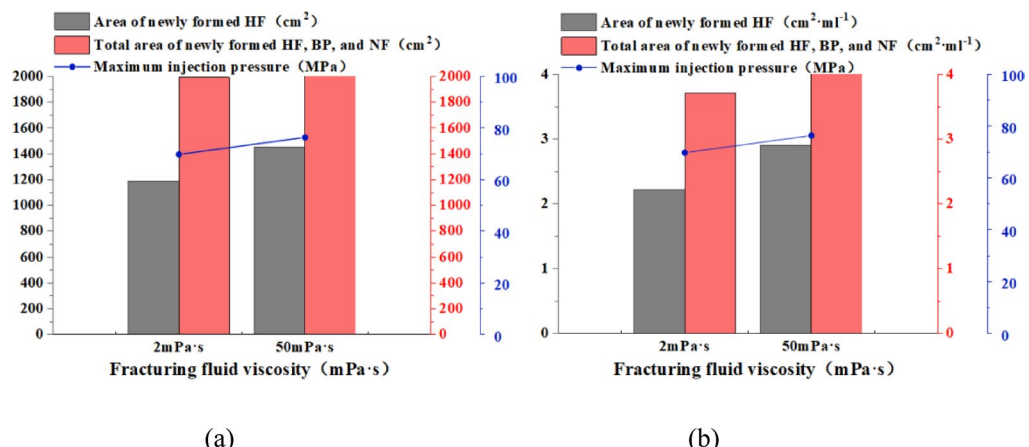


Fig. 20. Fluid viscosity effects on hydraulic fracturing efficiency. (a) Activated fracture area (b) Per-fluid-volume fracture area. Notes: HF = Hydraulic fractures; BP = bedding planes; NF = natural fractures.

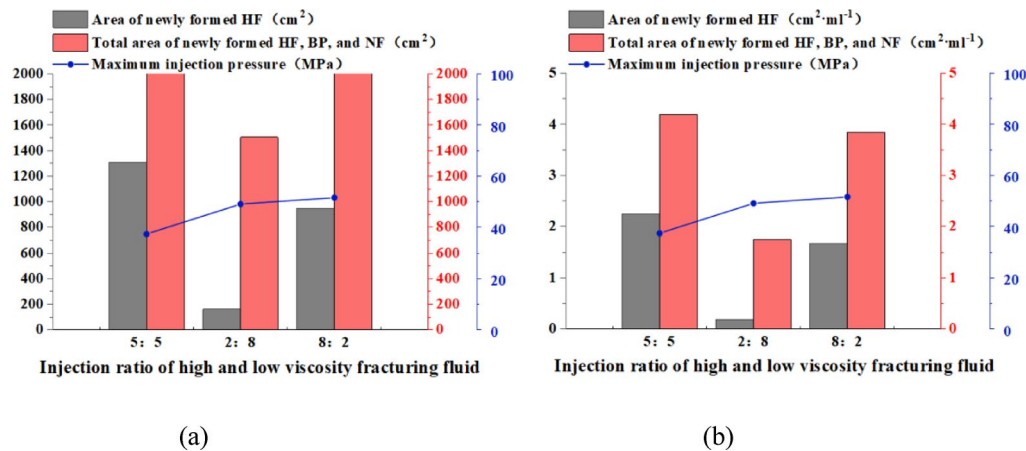


Fig. 21. Viscosity ratio effects on hydraulic fracturing efficiency. (a) Activated fracture area (b) Per-fluid-volume fracture area. Notes: HF = Hydraulic fractures; BP = bedding planes; NF = natural fractures.

stress conditions. This value corresponds precisely to one-third of the minimum horizontal principal stress (σ_h), presenting a unique mechanical signature in bedded shale with well-developed laminations. Previous studies have not considered the pressure variation under the condition of foliation fracture opening, nor its relationship with stress^{28–30}. In bedded shale, the dense laminations act as weak interfaces with lower shear strength and higher compliance compared to the matrix. Prior to fracture initiation, fluid pressure must first overcome the combined resistance from: (1) the minimum horizontal principal stress (σ_h); (2) the cohesive strength of bedding planes; and (3) the frictional resistance due to normal stress across laminations. The experimental data indicate that the 17 MPa increment specifically reflects the threshold for overcoming inter-bedding locking—this value is statistically consistent with the theoretical calculation of $\sigma_h/3$. This stability arises because the initial fracture initiation in bedded shale is dominated by the intrinsic mechanical anisotropy (bedding-controlled strength) rather than fluid rheology or stress magnitude variations. High-viscosity fluids enhance pressure transmission efficiency, while low-viscosity fluids promote bedding infiltration, but neither alters the fundamental threshold for breaking the inter-bedding cohesion. This finding advances prior knowledge by: identifying a quantifiable, bedding-dependent initiation pressure signature ($\sigma_h/3$) in laminar shale, which contrasts with the stress-proportional behavior in conventional reservoirs. Demonstrating that the first horizontal fracture in bedded shale represents a bedding unlocking event rather than simple matrix failure, providing a mechanistic basis for predicting initiation pressure in anisotropic formations. Offering a calibration metric for numerical models simulating shale fracturing, where bedding-plane interactions are often oversimplified. This consistent pressure increment serves as a critical indicator of the transition from fluid pressurization to effective fracture.

Figure 19a demonstrates that increasing injection rate elevates initial fracturing pressure, which promotes multi-fracture initiation and generates dominant hydraulic fractures. Experimental observations show four hydraulic fractures at 35 ml/min (Fig. 3) versus a single fracture at 50 ml/min (Fig. 7), with new fracture area at higher rates representing 54% of lower-rate values while maintaining equivalent total fracture dimensions. This inverse relationship between injection rate and fracture multiplicity indicates that elevated rates suppress near-wellbore fracture branching while enhancing primary fracture propagation. Correspondingly, Fig. 19b reveals improved stimulation efficiency through 23% increases in unit-fluid-volume fracture area under high-rate conditions, confirming that accelerated injection rates optimize hydraulic fracture development by overcoming near-wellbore constraints.

Figure 20a demonstrates that elevated fracturing fluid viscosity promotes new fracture initiation without significantly altering fracture initiation pressures or total fracture dimensions. Experimental results reveal a viscosity-dependent fracture density reduction from four fractures at 2 mPa·s to two fractures at 50 mPa·s, indicating that high-viscosity fluids suppress near-wellbore fracture branching while enhancing fracture propagation distance. The viscosity increase from 2 to 50 mPa·s improves unit-fluid-volume stimulation area by 12.8% (Fig. 20b), confirming two critical benefits of viscous fluids: (1) reduced fluid loss through bedding planes/natural fractures, and (2) optimized fracture network geometry through controlled fracture branching. This viscosity-dependent mechanism enhances fluid efficiency while maintaining reservoir stimulation effectiveness through directional fracture extension.

Experimental results demonstrate negligible maximum injection pressure variations across viscosity ratios (Fig. 21a). Fracture generation efficiency follows a distinct hierarchy: 5:5 high-low viscosity ratio produces 23% greater new fracture area than 8:2 ratios and 41% more than 2:8 ratios. Total fracture area measurements show comparable effectiveness between 5:5 and 8:2 ratios, both exceeding 2:8 ratios by 34–38%. The optimal 5:5 viscosity ratio enhances bedding plane connectivity and natural fracture activation, increasing stimulated reservoir volume through dual mechanisms: high-viscosity phases extend primary fractures while low-viscosity phases propagate secondary fracture networks. Unit-fluid-volume stimulation efficiency peaks under 5:5 conditions, exceeding 8:2 and 2:8 ratios by 15% and 28% respectively (Fig. 21b). This balanced viscosity approach generates 40–45% more hydraulic fractures than extreme ratio treatments while activating 2.3× more natural

discontinuities. The 5:5 ratio optimally combines the dual benefits of viscous fluid-driven fracture elongation and low-viscosity-enhanced fracture branching, achieving maximum reservoir contact through synergistic viscosity effects.

Prior homogeneous rock studies reported that high-viscosity fluids increase fracture width but could not resolve ratio-dependent synergy^{30,31}. Here, the 5:5 hybrid ratio maximizes fracture volume by balancing. This dual-phase mechanism—absent in homogeneous systems—explains why 5:5 outperforms single fluids, whereas earlier works attributed volume gains solely to viscosity magnitude. The 5:5 high-low viscosity ratio maximizes fracture volume through synergistic integration of primary fracture propagation and secondary network activation, overcoming limitations of single-fluid or extreme-ratio systems. Three fundamental mechanisms govern this optimization: (1) structural framework establishment and network infill synergy. High-viscosity fluid (50 mPa·s) generates sustained fracture-tip pressure through viscous resistance, driving primary fracture extension along maximum stress orientation. At 5:5 ratio, its concentration maintains adequate tensile stress for deep fracture penetration, establishing the fracture network's structural framework. Low-viscosity fluid (2 mPa·s) exploits reduced friction and capillary forces to infiltrate bedding planes and micro-fractures along primary fracture walls. The balanced ratio provides optimal concentration for secondary channel activation without over-dilution. Experimental measurements confirm that the 5:5 high-low viscosity ratio achieves the most balanced development between hydraulic fractures ($2.25 \text{ cm}^2 \text{ ml}^{-1}$) and activated bedding planes/natural fractures ($1.94 \text{ cm}^2 \text{ ml}^{-1}$). All other viscosity ratios exhibit area differentials exceeding $0.31 \text{ cm}^2 \text{ ml}^{-1}$. (2) Pressure-Flow field coupling optimization. Fracture volume depends on pressure-driven extension and fluid penetration coverage. The 5:5 ratio achieves optimal coupling through. ① Pressure field stability: high-viscosity components reduce fluid loss rates, maintaining above-initiation pressure for sufficient primary fracture propagation. ② Flow field penetration: controlled low-viscosity fractions prevent micro-fracture occlusion, enabling uniform activation of bedding planes while minimizing unstimulated zones. (3) Fluid efficiency maximization. The 5:5 ratio prevents inefficient fluid utilization observed in extreme ratios. 8:2 ratios waste energy through excessive primary fracture extension beyond productive zones. 2:8 ratios cause ineffective fluid leakage into non-target layers. This balanced approach integrates the fracture-extension capability of viscous fluids with the network-activation capacity of low-viscosity fluids, achieving optimal stimulation through synergistic mechanics-fluid dynamics integration.

Conclusion

This study clarifies shale fracture propagation mechanisms in bedded formations through systematic analysis of fracture geometry under varying geostress conditions and operational parameters. Fracture initiation pressure for the first horizontal hydraulic fracture measures 17 MPa, equivalent to one-third of the minimum horizontal principal stress. Four key parametric relationships emerge:

First, reduced minimum horizontal principal stress (47 MPa vs 51 MPa) decreases breakdown pressure by 53% (40 MPa vs 84.74 MPa) and shortens pressurization duration, demonstrating that lower horizontal stress facilitates fracture initiation. Vertical fractures form despite near-wellbore bedding planes under high stress differentials, justifying preferential fracturing target selection in high-stress-difference zones.

Second, elevated injection rates (35–50 ml/min) enhance fracture penetration through near-wellbore constraints, increasing fracture height by 159% (7.1–18.4 cm). High-rate operations achieve rapid pressure escalation and promote deep fracture propagation.

Third, increased fracturing fluid viscosity (2–50 mPa·s) reduces bedding-plane fluid loss and sustains fracture pressure, generating 52% taller fractures (7.1–10.8 cm). While viscosity elevation proves less effective than rate optimization for fracture extension, combining high-viscosity fluids with accelerated injection rates maximizes bedding-plane penetration.

Fourth, alternating high/low-viscosity fluids (5:5 ratio) optimizes fracture network complexity through synergistic mechanisms: high-viscosity phases establish primary fractures while low-viscosity phases activate bedding planes. This balanced approach increases stimulated reservoir volume by 23–28% compared to extreme viscosity ratios, effectively overcoming near-wellbore constraints through pressure maintenance and fracture branching. Viscosity ratio effects as novel control mechanism that significantly affects the propagation of fractures in reservoirs with well-developed bedding planes.

These findings establish an operational framework for laminated shale stimulation, emphasizing stress-differential targeting, rate-controlled fracture propagation, viscosity-modulated fluid efficiency, and optimized viscosity sequencing to maximize fracture network connectivity.

Limitations and future work

This study has potential limitation, while our results provide valuable insights into the spatiotemporal evolution of fractures under different conditions, the conclusions are derived from a limited set of samples and should be interpreted with consideration of natural variability. Sample heterogeneity limits direct comparisons, but our multi-parameter analysis (viscosity, injection rate, stress) offers a broader operational window for field applications. Future studies involving statistically significant sample sizes or advanced imaging techniques (e.g., digital rock modeling) could further validate these findings. Meanwhile, the cumulative energy, b-value analysis, and other quantitative AE metrics are insightful for microseismic characterization, We will incorporate these advanced AE analyses in subsequent research to further unravel fracture dynamics in heterogeneous shale.

Data availability

The data that support the findings of this study are available on request from the corresponding author. The data are not publicly available due to privacy or ethical restrictions.

Received: 11 March 2025; Accepted: 7 November 2025

Published online: 24 December 2025

References

1. Patel, S. M. et al. Hydraulic fracture permeability estimation using stimulation pressure data. *Int. J. Rock Mech. Min.* **101**, 50–53 (2018).
2. Su, Y. et al. Theoretical analysis of the mechanism of fracture network propagation with stimulated reservoir volume (SRV) fracturing in tight oil reservoirs. *PLoS ONE* **10**, e0125319 (2015).
3. Zhang, F. et al. Investigating hydraulic fracturing complexity in naturally fractured rock masses using fully coupled multiscale numerical modeling. *Rock Mech. Rock Eng.* **52**, 5137–5160 (2019).
4. Long, S. et al. Prospect analysis of the deep marine shale gas exploration and development in the Sichuan Basin, China. *J. Nat. Gas Geosci.* **3**, 181–189 (2018).
5. Zhang, X. et al. Structure- and lithofacies-controlled natural fracture developments in shale: Implications for shale gas accumulation in the Wufeng-Longmaxi formations, fuling field, Sichuan Basin. *China. Geoenergy Sci. Eng.* **223**, 211572 (2023).
6. Liu, K. et al. Experimental study of the effect of stress anisotropy on fracture propagation in eagle ford shale under water imbibition. *Eng. Geol.* **249**, 13–22 (2019).
7. Zhang, Q. et al. Geomechanical behaviors of shale after water absorption considering the combined effect of anisotropy and hydration. *Mar. Petrol. Geol.* **269**, 105547 (2020).
8. Gehne, S. et al. Fluid-driven tensile fracture and fracture toughness in Nash Point shale at elevated pressure. *J. Geophys. Res. Solid Earth* **125**, 1–11 (2020).
9. Guo, P. et al. Quantitative analysis of anisotropy effect on hydrofracturing efficiency and process in shale using X-ray computed tomography and acoustic emission. *Rock Mech. Rock Eng.* **54**, 5715–5730 (2021).
10. Guo, P. et al. Experimental study on hydrofracture propagation through perforated wellbore in naturally fractured Guanyinqiao calcareous mudstone under true triaxial stress. *J. Nat. Gas. Sci. Eng.* **99**, 104415 (2022).
11. Wang, J. et al. Anisotropic failure behaviour and breakdown pressure interpretation of hydraulic fracturing experiments on shale. *Int. J. Rock Mech. Min. Sci.* **142**, 104478 (2021).
12. Zhao, H. et al. Effect of hydrostatic pressure on hydraulic fracturing properties of shale using X-ray computed tomography and acoustic emission. *J. Petrol. Sci. Eng.* **215**, 110725 (2022).
13. Guo, P. et al. Experimental investigation of simultaneous and asynchronous hydraulic fracture growth from multiple perforations in shale considering stress anisotropy. *Rock Mech. Rock Eng.* **56**(11), 8209–8220 (2023).
14. Jiang, Y. et al. Experimental study of supercritical CO₂ fracturing on initiation pressure and fracture propagation in shale under different triaxial stress conditions. *J. Nat. Gas Sci. Eng.* **55**, 382–394 (2018).
15. Yang, S. et al. Experimental study on mechanical behavior and brittleness characteristics of Longmaxi formation shale in Changning, Sichuan Basin, China. *Rock Mech. Rock Eng.* **53**, 2461–2483 (2020).
16. Gehne, S. et al. Seismomechanical response of anisotropic rocks under hydraulic fracture conditions: New experimental insights. *J. Geophys. Res. Solid Earth* **124**, 9562–9579 (2019).
17. Zhao, Y. et al. A composite criterion to predict subsequent intersection behavior between a hydraulic fracture and a natural fracture. *Eng. Fract. Mech.* **209**, 61–78 (2019).
18. Zheng, H. et al. Study on the interaction between hydraulic fracture and natural fracture based on extended finite element method. *Eng. Fract. Mech.* **230**, 106981 (2020).
19. Morgan, S. P. et al. Cracking processes affected by bedding planes in opalinus shale with flaw pairs. *Eng. Fract. Mech.* **176**, 213–234 (2017).
20. Tan, P. et al. Analysis of hydraulic fracture initiation and vertical propagation behavior in laminated shale formation. *Fuel* **206**, 482–493 (2017).
21. Heng, S. et al. Experimental and numerical study on the non-planar propagation of hydraulic fractures in shale. *J. Petrol. Sci. Eng.* **179**, 410–426 (2019).
22. Gale, J. F. W. et al. Natural fractures in shale: a review and new observations. *AAPG Bull.* **98**, 2165–2216 (2014).
23. Guo, P. et al. Combined effect of in situ stress level and bedding anisotropy on hydraulic fracture vertical growth in deep marine shale revealed via CT scans and acoustic emission. *Energies* **16**, 7270 (2023).
24. Jiang, C. et al. CT-based reconstruction of the geometry and propagation of hydraulic fracture in shale. *J. Petrol. Sci. Eng.* **179**, 899–911 (2019).
25. Li, L. et al. A review of the current status of induced seismicity monitoring for hydraulic fracturing in unconventional tight oil and gas reservoirs. *Fuel* **242**, 195–210 (2019).
26. Stanek, F. et al. Seismicity induced by hydraulic fracturing in shales: A bedding plane slip model. *J. Geophys. Res. Solid Earth* **122**, 7912–7926 (2017).
27. Chen, H. et al. Microseismic monitoring of stimulating shale gas reservoir in SW China: 2. Spatial clustering controlled by the preexisting faults and fractures. *J. Geophys. Res. Solid Earth* **123**, 1659–1672 (2018).
28. Zou, Y. et al. Experimental investigation into hydraulic fracture network propagation in gas shales using CT scanning technology. *Rock Mech. Rock Eng.* **49**, 33–45 (2016).
29. Ma, X. et al. Hydraulic fracture propagation geometry and acoustic emission interpretation: A case study of Silurian Longmaxi formation shale in Sichuan Basin. *SW China. Pet. Explor. Dev.* **44**(6), 1030–1037 (2017).
30. Stanchits, S. et al. Onset of hydraulic fracture initiation monitored by acoustic emission and volumetric deformation measurements. *Rock Mech. Rock Eng.* **47**(5), 1521–1532 (2014).
31. Stanchits, S. et al. Hydraulic fracturing of heterogeneous rock monitored by acoustic emission. *Rock Mech. Rock Eng.* **48**(6), 2513–2527 (2015).

Acknowledgements

The authors acknowledge the support from Key R&D projects in Heilongjiang Province (JD2023GJ02).

Author contributions

Conceptualization: Xu Wei, and Meng Cai; Supervision: Meng Cai; Writing—original draft: Xu Wei, and Dezhao Zhao; Visualization and investigation: Cuilong Kong; Data collection: Dezhao Zhao; Writing—review and editing: Xu Wei, Meng Cai, and Cuilong Kong; All authors read and approved the final manuscript.

Declarations

Competing interests

The authors declare no competing interests.

Additional information

Correspondence and requests for materials should be addressed to X.W.

Reprints and permissions information is available at www.nature.com/reprints.

Publisher's note Springer Nature remains neutral with regard to jurisdictional claims in published maps and institutional affiliations.

Open Access This article is licensed under a Creative Commons Attribution-NonCommercial-NoDerivatives 4.0 International License, which permits any non-commercial use, sharing, distribution and reproduction in any medium or format, as long as you give appropriate credit to the original author(s) and the source, provide a link to the Creative Commons licence, and indicate if you modified the licensed material. You do not have permission under this licence to share adapted material derived from this article or parts of it. The images or other third party material in this article are included in the article's Creative Commons licence, unless indicated otherwise in a credit line to the material. If material is not included in the article's Creative Commons licence and your intended use is not permitted by statutory regulation or exceeds the permitted use, you will need to obtain permission directly from the copyright holder. To view a copy of this licence, visit <http://creativecommons.org/licenses/by-nc-nd/4.0/>.

© The Author(s) 2025